ABSTRACT

ADSORPTION OF PARTICLES ON FLUID-LIQUID INTERFACES

by
Bhavin Dalal

Particles floating on fluid-liquid interfaces are of considerable interest because of their importance in a range of physical applications and biological processes, e.g., self-assembly of particles at fluid-fluid interfaces resulting in novel nano structured materials, stabilization of emulsions, formation of pollen and insect egg rafts, etc. The aim of this dissertation is to explore the mechanism by which particles are adsorbed at fluid-liquid interfaces. It is shown that the inertia of a particle plays an important role in its motion in the direction normal to a fluid-liquid interface, and in determining the particles adsorption trajectory and orientation in the adsorbed state. Although the importance of inertia diminishes with decreasing particle size, on an air-water interface the inertia continues to be important even when the particle size is as small as a few nanometers.

This dissertation also investigates the vertical oscillations of a particle while it is being adsorbed on an interface. The fact that the particle oscillates vertically implies that its behavior is similar to that of an under-damped mass-spring-dashpot system, and that it has characteristic linear and rotational frequencies which depend on the physical properties of the fluids involved and those of the particle. The experimentally measured frequency of oscillation of a particle is in approximate agreement with the frequency calculated analytically, which is noteworthy considering that the latter depends only on the fluid and particle properties, and that there are no adjustable parameters in the

analytic expression. It is shown that similarly to an under-damped system, these characteristic frequencies can be excited by an external forcing.

When a particle is adsorbed on a fluid-liquid interface it induces a relatively strong transient flow in the liquid which persists for several seconds. For a spherical particle the flow is axisymmetric about the vertical passing through the particle's center. To visualize this flow, an experiment is designed based of the Particle Image Velocimetry (PIV) technique. The measurements show that the fluid directly below the particle rises up, and near the interface it moves away from the particle. The velocity near the interface is found to be about an order of magnitude larger than in the liquid below the particle.

ADSORPTION OF PARTICLES ON FLUID-LIQUID INTERFACES

by
Bhavin Dalal

A Dissertation
Submitted to the Faculty of
New Jersey Institute of Technology
in Partial Fulfillment of the Requirements for the Degree of
Doctor of Philosophy in Mechanical Engineering

Department of Mechanical and Industrial Engineering

May 2012

APPROVAL PAGE

ADSORPTION OF PARTICLES ON FLUID-LIQUID INTERFACES

Bhavin Dalal

Dr. Pushpendra Singh, Dissertation Co-Advisor — Date
Professor of Mechanical and Industrial Engineering, NJIT

Dr. Ian Fischer, Dissertation Co-Advisor — Date
Professor of Mechanical and Industrial Engineering, NJIT

Dr. I. J. Rao, Committee Member — Date
Associate Professor of Mechanical and Industrial Engineering, NJIT

Dr. Anthony Rosato, Committee Member — Date
Professor of Mechanical and Industrial Engineering, NJIT

Dr. Denis Blackmore, Committee Member — Date
Professor of Mathematical Sciences, NJIT

BIOGRAPHICAL SKETCH

Author: Bhavin Dalal

Degree: Doctor of Philosophy

Date: May 2012

Undergraduate and Graduate Education:

- Doctor of Philosophy in Mechanical Engineering,
  New Jersey Institute of Technology, Newark, NJ, 2012

- Master of Science in Mechanical Engineering,
  Bradley University, Peoria, IL, 2007

- Bachelor of Engineering in Mechanical Engineering
  Gujarat University, Gujarat, India, 2003

Major: Mechanical Engineering

Presentations and Publications:

P. Singh, I.S. Fischer, B. Dalal, S.K. Gurupatham, M.S. Hossain, and N. Musunuri, Spontaneous dispersion of particles on fluid-liquid interfaces. 24th ICTAM, 19-24 August (2012) Beijing, China.

B. Dalal, P. Singh, and S.K. Gurupatham, Improving the shear strength of the rheological liquid using external electric fields, in preparation (2012).

S. Gurupatham, M.S. Hossain, B. Dalal, I.S. Fischer, P. Singh, and D.D. Joseph, Breakup of particle clumps on liquid surfaces, Powder Technology, 217 (2012) 288–297

M.S. Hossain, B Dalal, S.K. Gurupatham, S. Nudurupati, M. Janjua, I.S. Fischer and P. Singh, Electric field induced self-assembly of monolayers of binary mixtures of particles. Submitted (2012).

B. Dalal, P. Singh, I. S. Fischer, and D. D. Joseph, The role of particle inertia in its motion in the direction normal to a fluid-liquid interface, Eighth Annual Conference on Frontiers in Applied and Computational Mathematics June 9-11, (2011) Newark, New Jersey.

M.S. Hossain, S. Pillapakkam, B. Dalal, I.S. Fischer, P. Singh, and N. Aubry, Modeling of blood flow in the human brain. ASME 2011 International Mechanical Engineering Congress & Exposition, IMECE2011-64525 Nov 11-17 (2011) Denver, Colorado.

S. K Gurupatham, M.S. Hossain, B. Dalal, I.S. Fischer, P. Singh, D.D. Joseph, Spreading of solid powder particles over liquid surfaces, Powder Technology (2011).

P. Singh, D. D. Joseph, I. S. Fischer, and B. Dalal, Role of particle inertia in adsorption at fluid-liquid interfaces. Submitted to Physics Review Letters (2011).

S.K. Gurupatham, B. Dalal, M.S. Hossain, I.S. Fischer, P. Singh, and D.D. Joseph, Particles dispersion on fluid–liquid interfaces, Particuology, 9.1 (2011) 1-13

B. Dalal, S.K. Gurupatham, M. S. Hossain, I.S. Fischer, and P. Singh, Dispersion of Particles on Fluid-Liquid Interfaces, 64th Annual Meeting of the APS Division of Fluid Dynamics, DFD11-2011-000083, November 20-22 (2011) Baltimore, MD.

S. K. Gurupatham, M.S. Hossain, B. Dalal, I.S. Fischer, and P. Singh, Breakup of particle clumps on liquid surfaces, 64th Annual Meeting of the APS Division of Fluid Dynamics, DFD11-2011-000082, November 20-22 (2011) Baltimore, MD

M.S. Hossain, B. Dalal, S.K. Gurupatham, I.S. Fischer, and P. Singh, Electric field induced self-assembly of particles at liquid-liquid interfaces, 64th Annual Meeting of the APS Division of Fluid Dynamics, DFD11-2011-000113, November 20-22 (2011) Baltimore, MD

S.K. Gurupatham, B. Dalal, M.S. Hossain, I.S, Fischer, and P. Singh, Breakup of particle clumps on liquid surfaces, Eighth Annual Conference on Frontiers in Applied and Computational Mathematics June 9-11 (2011) Newark, New Jersey.

M.S. Hossain, B. Dalal, I.S. Fischer, P. Singh, and N. Aubry, Modeling of blood flow in the human brain, Eighth Annual Conference on Frontiers in Applied and Computational Mathematics June 9-11 (2011) Newark, New Jersey.

S.K. Gurupatham, M. Hossain, B. Dalal, I.S. Fischer, P. Singh, and D.D. Joseph, Breakup of particle clumps on liquid surfaces, 63rd Annual Meeting of the APS Division of Fluid Dynamics Volume 55, Number 16, November 21–23 (2010) Long Beach, California.

S.K. Gurupatham, B. Dalal, M. Hossain, I.S. Fischer, P. Singh, and D.D. Joseph, Particle dispersion at fluid liquid interface, 63rd Annual Meeting of the APS Division of Fluid Dynamics Volume 55, Number 16, November 21–23(2010) Long Beach, California.

S.K. Gurupatham, B. Dalal, I.S. Fischer, S. Nudurupati, P. Singh, and D.D. Joseph, Spontaneous Dispersion of Particles on Liquid Surfaces, ASME 2010 Fluids

Engineering Summer Meeting , (FEDSM-ICNMM2010-30555) August 1-5 (2010) Montreal, Canada.

M.S. Hossain, B. Dalal, I.S. Fischer, P. Singh, and N. Aubry, Modeling of blood flow in the human brain, 8th International Conference on Nanochannels, Microchannels and Minichannels , ASME 2010 Fluids Engineering Summer Meeting (FEDSM-ICNMM2010-30554) August 1 - 5 (2010) Montreal, Canada.

S.K. Gurupatham, B.Dalal, S. Nudurupati, I.S. Fischer, P. Singh, and D.D. Joseph, Spontaneous dispersion of particles on liquid surfaces, 16th US National Congress on Theoretical and Applied Mechanics (USNCTAM) June 27 - July 2 (2010) State College, PA.

M. S. Hossain, B. Dalal, I.S. Fischer, P. Singh and N. Aubry, Modeling of blood flow in the human brain, 16th US National Congress on Theoretical and Applied Mechanics (USNCTAM) June 27 - July 2 (2010) State College, PA.

B. Dalal, S. Gurupatham, M. Janjua, S. Nudurupati, I.S. Fischer, P. Singh and N. Aubry, Electric field induced self-assembly of particles on fluid interface, Seventh Annual Conference on Frontiers in Applied and Computational Mathematics (FACM) May 21-23 (2010) Newark, New Jersey.

S.K. Gurupatham, B. Dalal, S. Nudurupati, I.S. Fischer, P. Singh, and D.D. Joseph, Spontaneous dispersion of particles on Air water interface, Seventh Annual Conference on Frontiers in Applied and Computational Mathematics(FACM) on May 21-May 23 (2010). Newark, New Jersey.

P. Singh, D.D. Joseph, S.K. Gurupatham, B.Dalal, and S. Nudurupati, Spontaneous dispersion of particles on liquid surfaces, PNAS, 0910343106 (2009) .

Dedicated to my family

ACKNOWLEDGMENT

I would like to thank my committee beginning with Dr. Pushpendra Singh, my mentor and co-advisor, who inspired me, encouraged me, strengthened me, organized me, and helped put me on the path to this Ph.D. I also wish to thank my co-advisor Dr. Ian Fischer, who brought an assortment of simply brilliant ideas along the way. I owe a great debt of gratitude not only to Dr. Singh and Dr. Fischer but also to the rest of my committee: Dr. I. Joga Rao, Dr. Anthony Rosato, and Dr. Denis Blackmore for their efforts on my behalf. I appreciate the unique perspectives of each of my committee members. My committee members never strayed from their commitment to see me through my dissertation process successfully. I appreciate Dr. Rao's kindness and peaceful presence and Dr. Rosato's sense of humor and general interest in my welfare. I appreciate Dr. Blackmore's efforts in advising someone outside of his department. I can say without hesitation that I benefitted a lot from their vast knowledge of Mechanical Engineering and Mathematics.

I would like to thank all professors at NJIT who taught me. Thank you to Dr. Rao for your challenging and exciting courses in Continuum Mechanics. Thank you to Dr. Chao Zhu for pushing me to work hard in your Multiphase Flow Course. Thank you to Dr. Singh for the theoretical background delivered in your Fluid Mechanics and Advance Finite Element courses.

I would like to express my gratitude to the staff of the Department of Mechanical and Industrial Engineering for their support. Thank you to Mr. Joseph Glaz, Mr. Gregory Policastro, and Mr. Jack Gidney. Special acknowledgement should be made to Mr. Glaz and Mr. Policastro for their work in the creation of multiple devices and various

equipments used in my experiments. They also gave me valuable tips on using and selecting multiple tools, machines, and equipment. I will always remember the first toolbox I bought based on Mr. Glaz's recommendation. I wish to also thank Ms. Barbara J. Valenti, Ms. Yvonne Williams, and Ms. Aileen Checa for helping me in numerous ways. I also wish to thank Ms. Helen Gramcko, the Director of Operations of the York Center, where I conducted my experiments. Ms. Gramcko took interest in both my professional and personal accomplishments and I will always remember her kindness.

I would like to give a special thank you to my senior colleagues, Dr. Muhammad Mansoor Janjua, Dr. Sai C. Nudurupati, and Dr. Sathishkumar Gurupatham for their experimentation provided the background to this research. Also thank you to my junior colleagues, Mr. Shahadat Hossain, Mr. Naga Aditya Musunuri, and Mr. Andrew Salerno for your assistance and input; I wish you luck as you continue your education at NJIT.

I would also like to acknowledge my other classmates and friends for their support: Dr. Jaskirat Sodhi, Dr. Mahesh Khanolkar, and Ms. Neha Chang.

I must express gratitude to the International Students Office, the NJIT Librarians, and the Graduate Studies Office. Thank you to the staff of the International Students Office for always helping in a timely manner. Thank you librarians for helping to access the articles and books I needed. Thank you to Ms. Clarisa González-Lenahan and Dr. Marino Xanthos of the Graduate Studies Office for their advice and editing especially in the final stages of this dissertation. The valuable suggestions made my Dissertation appear as professional as it is.

I would like to thank Dantec Dynamics, Edmund Optics and TSI Incorporated for their support in my Particle Image Velocimetry work as well. Special thanks to Evan from Trek Incorporation, for answering my questions. I would like to thank the vendors for their free samples of particles and fluids: 3M Corporation, Cospheric LLC, Dow Corning Corporation, Dupont Corporation, Dyneon Fluoroplastics, Epoxies Inc, Evonic Industries, Mo-Sci Corporation, PQ Corporation, and Potter Industries.

Words cannot express just how grateful I am to my family in India. I am forever indebted to my parents. They gave me a wonderful start to this life and continued guidance and support, financially, and emotionally. They raised me and pushed me in the right directions to lead me to this path. My mother would stay up late at night while I studied just in case I needed tea or food. My father would listen patiently as I talked out loud to come up with my own conclusions about mechanical engineering even though he knew the answers. I appreciate my younger brother for always reminding me to do my best, for always supporting me, always making me laugh, and admiring me even when I fail. I thank my neighbors for visiting my home to discuss engineering with my father when I was young for they provided the earliest sparks in my interest for my career. I wish to thank my aunts, uncles, and cousins in India for celebrating with me all my accomplishments.

I also must express my appreciation to my family in the United States. Thank you to my wife, for her support, patience, proofreading, editing, and love throughout my PhD studies. She made some of the best lunch sandwiches so that I can work without taking breaks. Thank you to my daughter; she does not know how much she has helped me this past year since she was born. I am very grateful to my mother in law for staying home

with my daughter. Her love for her granddaughter, daughter, and me relieved a great deal of stress and guilt from this process. Thank you to my sister in law and her husband and my brother in law, his wife, and his daughter for accepting me into your family and taking an interest in my studies and my life. I appreciate the spontaneous get-togethers, dinners, and friendship. Thank to you my cats, Captain and Braky, for waking me up in the morning, keeping me company when I am sick, and entertaining me for hours with your playfulness. Without my family here, my life would not be so rich and complete.

I wish to thank my friends. Thank you to Nikhil and Kunal, who have been with me since the beginning of my career. I admire you for your intellect and work habits for they are so similar to my own. Thank you also to Scott, who I admire for his teaching me so much practical knowledge in Mechanical Engineering while building ours rigs in a cost efficient albeit labor intensive manner. Thank you to the members of my local New Jersey Jeep Association for your support on and off the road. I would be still stuck if not for them; you provide me with valuable knowledge, inspiration to graduate and relieve stress.

I would also gratefully acknowledge the financial support of the National Science Foundation. In addition, I would like to acknowledge my other sources of funding. Thank you to Department of Mechanical and Industrial Engineering and Dr. Zhiming Ji for employing me as a Teaching Assistant. I would like to thank the professors that I worked under as their Teaching Assistant: Dr. Pushpendra Singh, Dr. Avraham Harnoy, Prof. Ben Serico, Prof. Giorgioni, Dr. Chao Zhu, Dr. Surjanhata Herli, Prof Mohammad Behi and Prof. Balraj Mani. For my Adjunct Professor appointment in the Engineering Technology Department, I want to thank Dr. Herli Surjanhata for recommending me and

for Dr. Thomas Juliano for hiring and advising me. I would also like to thank all the students who took all these classes, especially the ones with inquisitive minds making classes interesting and challenging, inspiring me to continue my career in teaching.

Finally, I express my thankfulness to the scholarly community. I am inspired by the creativity and genius of my peers around the world.

TABLE OF CONTENTS

Chapter			Page
1	INTRODUCTION		1
	1.1	Introduction	1
	1.2	Forces on Floating Particles	7
		1.2.1 Lateral Forces on a Particle	10
		1.2.2 Vertical Force Balance	11
	1.3	Thesis Organization	12
2	ADSORPTION OF A PARTICLE ON A FLUID-LIQUID INTERFACE		14
	2.1	Introduction	14
	2.2	Momentum Conservation	17
		2.2.1 Brownian Forces	20
		2.2.2 Governing Dimensionless Parameters	21
	2.3	Vertical Oscillation of a Sphere	24
		2.3.1 Vertical Oscillation of a Particle During Adsorption	27
	2.4	Rotational Oscillation of a Rod	30
	2.5	Particle Velocity During Adsorption	31
	2.6	Conclusion	33
3	FORCED OSCILLATIONS OF PARTICLES ON FLUID-LIQUID INTERFACES		34
	3.1	Forcing Frequency	34
4	EXPERIMENTAL SETUP AND RESULTS FOR FORCED OSCILLATIONS		39
	4.1	Experimental Setup	40
	4.2	Description of the Experiment	42
	4.3	Results	43
		4.3.1 Particle on Air-Water Interface	44
		4.3.2 2 mm Particle on Corn-Oil Water Interface	48
		4.3.3 Frequency as a Function of Particle Diameter	49

TABLE OF CONTENTS
(Continued)

Chapter			Page
5	DISPERSION OF PARTICLES ON FLUID-LIQUID INTERFACES		50
	5.1	Fluid Motion Induced at the Interface	50
	5.2	Lateral Motion of Particles	53
6	FLOW VISUALIZATION AND MEASUREMENT		58
	6.1	Introduction	58
	6.2	Brief History of PIV	59
	6.3	Experimental Setup and Components of PIV System	61
		6.3.1 Experimental Setup	61
		6.3.2 Camera	62
		6.3.3 Laser	63
		6.3.4 Seeding Particles	64
		6.3.5 Measurement Technique	65
		6.3.6 Interrogation Area and Velocity Distribution	66
		6.3.7 Cross Correlations and the FFT Approach	67
		6.3.8 Image Intensity Field	68
		6.3.9 Cross-Correlation of Two Images	68
		6.3.10 PIVLAB	70
	6.4	Experimental Results	71
		6.4.1 Velocity Distribution	72
		6.4.2 Transient Velocity Distribution	77
		6.4.3 Time Variation of Velocity Near a Test Particle	85
7	CONCLUSIONS		89

LIST OF FIGURES

Figure **Page**

1.1 Sudden dispersion of particles sprinkled on to water in a Petri dish. In the left figure streak lines formed due to the radially outward motion of the flour particles emanating from the location where it was sprinkled can be seen. Approximately 1 s later, almost the entire water surface was covered by a layer of dispersed flour particles 5

1.2 When a test particle is dropped on the interface it moves smaller tracer particles away from itself. This creates a clear water surface around the test particle. The test particle was mustard seed and the tracer particles were 100 μm sized glass particles 5

1.3 Schematic of a heavier than liquid hydrophilic (wetting) sphere of radius *a* hanging on the contact line at θ_c. The point of extension of the flat meniscus on the sphere determines the angle θ_1 and h_2 is defined as $h_2 = R\,(\cos\theta_c - \cos\theta_1)$. The angle α is fixed by the Young-Dupré law and θ_c by the force balance 8

2.1 Vertical oscillation of a particle adsorbed at an air-liquid interface. The contact angle is assumed to be 90°, and so in equilibrium a small particle floats with its center at the undeformed interface. (a) The particle is pushed up from its equilibrium position in the interface. (b) The particle is pulled downwards by the interfacial force (γ). (c) The particle oscillates about the equilibrium height within the interface causing a radially outward secondary flow on the interface. (d) After oscillations subside, the particle assumes its equilibrium position..... 16

2.2 Vertical oscillation of a particle adsorbed at an air-liquid interface. The contact angle is assumed to be 90°, and so in equilibrium it floats with its center at the undeformed interface. (a) The particle is pushed up from its equilibrium position. (b) The particle is pulled downwards by the interfacial force (γ). (c) The particle oscillates about the equilibrium height. (d) After oscillations subside, the particle assumes its equilibrium position 16

2.3 Schematic of a heavier-than-liquid hydrophilic (wetting) sphere hanging on the contact line at θ_c. The point of extension of the flat meniscus on the sphere determines the angle θ_1 and h_2..... 18

LIST OF FIGURES
(Continued)

Figure **Page**

2.4 Rotational oscillation of a cylindrical rod adsorbed at an air-liquid interface. The contact angle is assumed to be 90°, and so in equilibrium the rod floats with its center at the undeformed interface and axis parallel to the interface. (a) The rod is rotated clockwise from its equilibrium orientation. (b) The rod rotates in the direction of the torque, but is pulled back by the interfacial torque towards its equilibrium orientation. (c) The rod oscillates about the equilibrium orientation. (d) After the oscillations subside, the rod assumes equilibrium orientation 20

2.5 The z-coordinate of the particle center obtained numerically by solving Equation. (2.4) is shown as a function of time. The particle oscillates about the equilibrium position (z=0) before coming to rest. The amplitude of oscillations decreases with increasing time. The parameters are the same as in figure 2.3 [2]. 23

2.6 The frequency (ω) of oscillation of the solution given by Equation (2.14) is plotted as a function of the particle radius. The parameter values were assumed to be: $\mu = 0.001$ Pa.s, $\rho_p = 1000.0$ kg/m^3, $\rho_p - \rho_c = 0.1$ kg/m^3 and $\gamma_{12} = 0.07$ N/m 25

2.7 Trapping of a spherical plastic bead of 2 mm diameter on the decane-water interface. The bead oscillated about its equilibrium position before its motion stopped. The sequence shows the phenomenon from the time the bead touched the interface to the time it reached the equilibrium position 27

2.8 The velocity of a spherical particle normal to the interface given by Equation (2.4) is plotted as a function of the particle radius. The parameter values are the same as in Figure 2.5 30

4.1 Schematic of the experimental setup used to study the forced oscillations of a steel bead floating on a liquid surface. An oscillating voltage from a function generator was amplified and then applied to an electromagnet mounted directly above the interface to produce an oscillating magnetic field. The bead was subjected to this oscillating magnetic force in the direction normal to the interface. The vertical oscillations of the bead were recorded using a high speed camera 17

4.2 Plot of amplitude of oscillation vs. frequency for 632 μm particle on air water interface 29

LIST OF FIGURES
(Continued)

Figure **Page**

4.3 Plot of amplitude of oscillation vs. frequency for 500 μm particle on air water interface..... 31

4.4 Plot of amplitude of oscillation vs. frequency for 2 mm bead on air water interface..... 31

4.5 Plot of amplitude of oscillation vs. frequency for 2 mm bead on Corn Oil water interface..... 49

4.6 Plot of natural frequency vs. diameter of particle on air water interface..... 53

5.1 The velocity of tracer particles on the air-water interface is plotted as a function of the distance (d) from the center of a glass test particle. The velocity distribution plotted here was recorded at a time 0.033 s after the particle was trapped at the interface. The data were taken for 7 different test particles of the same approximate diameter of 850 μm..... 55

5.2 The velocity of a tracer particle on the air-water interface initially at a distance of 2.05 mm from a glass test particle of diameter 850 μm is shown as a function of time. The velocity became negligibly small at t = ~0.8 s..... 56

5.3 The distance traveled by tracer particles on the air-water interface is plotted as a function of their initial distance from the glass test particle. The diameter of the test particle was 850 μm and that of the tracer particle was 100 μm 56

5.4 The velocity of tracer particles on the air-water interface is plotted as a function of the distance (d) from the mid-point of the line joining the centers of the two test particles. The diameter of the particles was 850 μm and the initial distance between them was 0.91 mm. The velocities shown here were recorded at a time of 0.033 s after the particles were trapped at the interface. The velocities of the tracer particles are shown along the directions inline (parallel) and perpendicular to the line joining the centers of the particles 70

5.5 The velocity of two glass particles of diameter 850 μm dropped simultaneously onto the air-water interface is shown as a function of time. The initial distance between the particles was 1.21 mm. After becoming trapped in the interface, they moved apart approximately along the line joining their centers. The magnitude of the velocities of the two particles was approximately equal 72

LIST OF FIGURES
(Continued)

Figure **Page**

5.6 The velocities of four glass particles simultaneously dropped onto an air-water interface. The particles moved apart approximately along radial lines emanating from the center of the four particles. The diameter of particles was 650 μm. The initial average distance between the four particles was around 1.0 mm 73

5.7 The average velocity with which glass particles moved apart 0.033 s after coming in contact with an interface as a function of the number of particles. The case marked "1" is for 850 μm glass particles sprinkled on water, "2" is for 650 μm glass particles sprinkled on 60% glycerin in water, and "3" is for 650 μm glass particles sprinkled on corn oil 79

5.8 The lateral velocity of the particles is shown as a function of time. The parameters are the same as in figure 19. The cases shown are: (i) Two particles released together at a height of 0.95*R* above the undeformed interface. The initial distance between the particles was 3.2*R*. (ii) Four particles released together at a height of 0.95*R* above the undeformed interface. The initial positions of the four particles formed the vertices of a square with sides 3.2*R*. (iii) One particle released at a height of 0.95*R* above the undeformed interface, and the center of the second one was at the undeformed interface. The horizontal distance between the particles was 3.2*R*. The velocity of the latter particle is shown while the velocity of the particle released above the undeformed interface was negligible 71

6.1 Schematics of the experimental setup. The laser sheet is perpendicular to the interface as well as the camera axis. The test particle is dropped along the line joining the axis of the camera and the laser 62

6.2 Schematic of the setup used to illuminate a plane with laser light. A combination of the spherical and cylindrical lenses produces a thin laser sheet as seen in the top view. The laser sheet expands at an angle of 20 degrees as it comes out of the cylindrical lens 65

6.3 Velocity distribution 0.3 s after a test particle touches the interface. The figure shows the seeded particles and the air water interface 68

LIST OF FIGURES
(Continued)

Figure **Page**

6.4 Schematics of the experimental setup. The laser illuminates fluid on a thin plane. The camera records frames at the required frame rate. The PIVlab algorithm selects the interrogation area in the frame and determines the velocity distribution within the frame. 72

6.5 Velocity field 0.383 s after a 2 mm glass particle came in contact with the air-water interface. The particle was dropped such that its center was approximately in the middle of the laser plane. The velocity distribution is approximately axisymmetric about the vertical passing through the center of the particle. 74

6.6 Velocity of the flow field. The fluid rises from the below towards the particle, as it comes close to the interface it moves away from the particle along the interface 75

6.7 Represents the x and y axis along which the data is plotted 76

6.8 Fluid velocity plotted as a function of distance from the center of the particle. The figure shows velocity 0.5 s after the particle came in contact with the interface 77

6.9 A time sequence of frames showing the fluid velocity distribution as a function of time. The parameters are the same as in Figure 6.5. The velocity vectors are shown on a vertical plane passing though the center of the particle. The flow is axisymmetric about the vertical line passing through the particle center. The velocity magnitude is shown by the lengths of the arrows. The video was recorded at a frame rate of 60 fps. The time shown in the figure is the time elapsed after the particle comes in contact with the interface. The sequence of frames a-k are shown next. 80

6.10 Time variation of the fluid velocity near a newly adsorbed test particle. The parameters are the same as in Figure 6.5. (a) The velocity at point A, (b) the velocity at point B and (b) the velocity at point C. The points are marked in Figure 6.9. The fluid velocity at each of the points quickly increases to a maximal value and then slowly decreases with time. 88

CHAPTER 1

INTRODUCTION

1.1 Introduction

The behavior of particles trapped at gas-liquid interfaces has come under intense scrutiny in recent years because of their importance in a wide range of applications, such as in waste-water treatments [1], mineral and solvent extractions processes [2], sorption of colloidal particles onto an air-water interface for generating films [3], preparation of anti-stick surfaces [4], separation of ink and toner particles [5], self-assembly of particles at fluid–fluid interfaces [6-14], stabilization of emulsions [5], pollination in hydrophilous plants [15], flotation of insect eggs [8,16,17], dispersion of viruses and protein macromolecules [8], pharmaceutical [18-21] and food industries [22].

The mechanics by which particles are captured and move on fluid-liquid surfaces (either gas-liquid or liquid-liquid interfaces), and their subsequent interactions leading to self assembly into monolayered patterns is very interesting. Particles captured on a liquid surface may be colloidal or non-colloidal. When a particle comes in contact with a fluid-liquid interface it is pulled inwards to its equilibrium position within the interface by the vertical component of the capillary and gravity forces [23]. The equilibrium position of an adsorbed particle in the interface is determined by the balance of the particle's buoyant weight, the vertical capillary force and any other force (with a vertical component) that acts on the particle. The particle is in stable equilibrium in the sense that if it is moved away from its equilibrium position, a restoring capillary force acts to bring it back. However, if the capillary force is not sufficiently large to overcome the buoyant weight, a

balance of the forces in the direction normal to the interface is not possible and the particle is not trapped in the interface. This is normally the case for millimeter and larger sized particles that are heavier than the liquid below. Micron and nano sized particles, on the other hand, for which the buoyant weight is negligible compared to the capillary force are readily trapped at the interface.

The strength of the force holding a particle at the interface can be quantified in terms of the interfacial energy released due to its trapping [23-26]. It can be shown that when the deformation of the interface due to the presence of the particle is negligible, which is the case for micron and nano particles, the adsorption energy, i.e., the decrease in the interfacial energy due to the adsorption of a spherical particle of radius R is given by,

$$W_a = \pi R^2 \gamma (1+\cos\alpha)^2 \tag{1.1}$$

where α is the contact angle, as defined by Young-Dupré law: $\cos\alpha = \frac{\gamma_{p2} - \gamma_{p1}}{\gamma}$, and γ_{pi} is the surface tension between the ith fluid and the particle, and γ is the interfacial tension between the upper and lower fluids. For larger heavier particles, the interface between the two fluids deforms to balance the buoyant weight of the particles, which increases the area between the two fluids, and thus, the adsorption energy holding them at the interface is smaller than the above value.

Since the adsorption energy W_a decreases with decreasing particle radius, the Brownian force on a trapped particle, which arises because of the random thermal

fluctuations in the fluid, can cause a small particle to de-adsorb. However, this cannot happen when W_a is much larger than kT, where k is the Boltzman constant and T the temperature. Therefore, since W_a decreases as the square of the particle radius, smaller particles can be dislodged more easily from the interface. For example, on the air-water interface if the contact angle is 90°, for R=10 μm, $W_a = 10^9\ kT$; for R=100 nm, $W_a = 10^5\ kT$; and for R=1 nm, $W_a = 10\ kT$. Therefore, since for R>100 nm the adsorption energy is several orders of magnitudes larger than kT, the capillary force holding such particles within the interface is much stronger than the Brownian force, and thus the adsorption of such particles at the air-water interface is essentially irreversible.

It was recently shown by [8] that when particles are sprinkled onto liquid surface they explosively disperse. The following simple experiment can be conducted in any household kitchen. Fill a bowl with water and wait for the water to settle down. Then sprinkle a pinch of wheat flour on the water surface. The flour particles will disperse as soon as they touch the surface of water (see Figure. 1.1). The force causing dispersion is so strong that a few milligrams of flour covers full surface of water almost instantaneously.

As discussed in detail below, particles sprinkled onto a liquid disperse because each of the newly adsorbed particles causes a flow away from itself on the interface. Therefore, when two or more particles are sprinkled onto a liquid surface, each of them causes the other particles to move apart. Experiments were conducted to understand the mechanism by which the radially outward flow arises and measure its strength for to a single spherical particle dropped onto a liquid surface. Throughout this dissertation, the dropped particle is called a test particle. The test particle itself, of course, does not move

laterally on the interface. To investigate the fluid motion caused by a test particle, the interface was seeded with 100 μm sized glass particles, as shown in Figure 1.2. Since the size of these seeded particles was much smaller than that of the test particle, it may be assumed that they acted approximately as tracer particles and their motion can be used to deduce the local fluid velocity caused by dropping a larger particle. This Figure shows that there is a clear fluid region around the test particle which indicates that its adsorption caused a flow on the interface which was away form the particle. The magnitude of the radially outward flow caused due to the adsorption of a test particle onto the air-liquid and liquid-liquid interfaces was measured for a range of particle sizes in [8,18].

When a particle comes in contact with a liquid surface the vertical capillary force acts to bring the particle to its equilibrium height within the interface. Therefore, for example, if the equilibrium height of a spherical particle is such that its center is at the undeformed surface, the particle must travel a distance equal to its radius downwards to reach equilibrium. The vertical capillary force that moves the particle towards the equilibrium height can accelerate the particle to a relatively large velocity normal to the interface. Also, the motion of the particle is dominated by inertia, and may overshoot its equilibrium height. The viscous drag force causes the particle to slow down, but it is not large enough to stop the particle as its momentum carries it beyond the equilibrium height. When this happens, the capillary force reverses direction and acts in the same direction as the drag. Hence, after moving down some additional distance, the particle reverses its direction. The vertical motion of the particle gives rise to a lateral flow on the interface away from the particle.

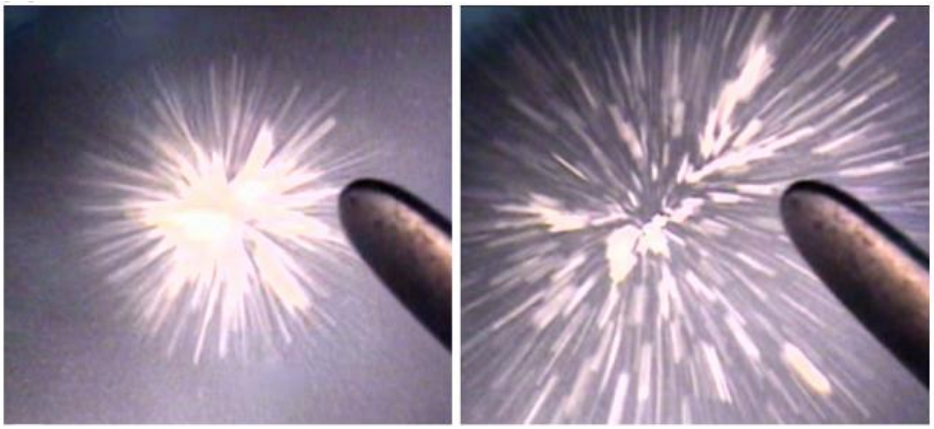

t=0.033 s t=0.067 s

Figure 1.1 Sudden dispersion of particles sprinkled on to water in a Petri dish. In the left Figure streak lines formed due to the radially outward motion of the flour particles emanating from the location where it was sprinkled can be seen. Approximately 1 s later, almost the entire water surface was covered by a layer of dispersed flour particles.

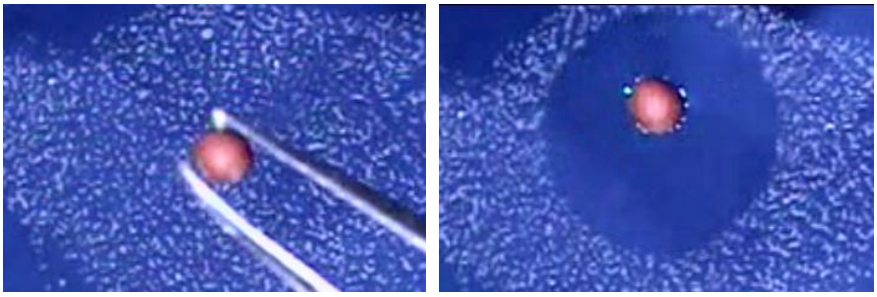

Figure 1.2 When a test particle is dropped on the interface it moves smaller tracer particles away from itself. This creates a clear water surface around the test particle. The test particle was mustard seed and the tracer particles were 100 μm sized glass particles.

This relatively violent phase, which lasts for a short period of time (about one second or less on mobile liquids) and is followed by a phase that is dominated by attractive lateral capillary forces during which particles slowly come back to cluster [27-35]. However, once micron- and nano-sized particles are dispersed, they may remain dispersed since for the attractive capillary forces are insignificant. Small particles may

experience other lateral forces, e.g., electrostatic, Brownian, etc., which may cause them to cluster or form patterns [36- 40].

A common example of capillarity-driven self-assembly is the clustering of breakfast cereal flakes floating on the surface of milk. The deformation of the interface due to the trapped particles, as they are heavier than milk, gives rise to lateral capillary forces which cause the flakes to cluster. The floating cereal particles experience attractive capillary forces due to the fact that when two such particles are close to each other, the interface height between the particles is lowered due to the interfacial tension. This lowering of the interface between the particles gives rise to lateral forces that cause them to come together. Another example of capillarity-induced motion is that of tea leaves floating on the liquid surface move towards the wall of the cup due to the formation of a meniscus that rises near the wall. This results in a net capillary force which pushes the lighter tea leaves towards the wall. The meniscus rises near the wall because the water wets the cup. If, on the other hand, the liquid does not wet the cup, i.e., the meniscus falls near the cup wall, particles lighter than the liquid tend to move away from the wall and migrate toward the center of the cup.

The modeling of interactions among floating particles is a formidable challenge because of the enormous complexity of the interactions and forces involved, i.e., the fluid dynamics of the interface motion, the contact-angle condition on the particles' surface and the contact-line motion, etc.[8, 35] Recently, a DNS approach was developed for particles trapped at fluid-fluid interfaces [8]. The approach provides not only a capability of resolving the motion of each particle as well as clusters of particles, but also the ability to address the particles' rapidly-changing dynamics. It is necessary to resolve the

particle-level details for particles trapped at fluid-fluid interfaces because the deformation of the interface in between the particles determines the strength of the lateral capillary forces between them, the latter being one of the main driving forces for their motion.

1.2 Forces on Floating Particles

The vertical component of the capillary force at the line of contact of the three phases on the particle surface is essential for keeping a heavier particle floating (see Figure 1.3). In fact, if the interfacial tension of the fluid-fluid interface is zero and the density of the particle is greater than that of the lower liquid, the particle would not be able to float at the interface and would actually sink. A particle with the density smaller than that of the lower liquid and larger than that of the upper liquid can of course float, but this is due to the buoyancy force.

The contact angle between the three phases at the line of contact is important because it, along with other parameters, determines the vertical component of the interfacial force. The three-phase contact angle on the surface of a floating spherical particle in equilibrium is given by the Young-Dupré law [8],

$$\gamma \cos \alpha = \gamma_{PG} - \gamma_{PL}, \tag{1.2}$$

where α is the contact angle and γ, γ_{PG} and γ_{PL} are the interfacial energy between liquid and gas, solid and gas, and solid and liquid, respectively. The Equation 1.2 implies that the interface near a smooth (particle) surface must adjust to meet the contact angle condition. This may require a motion of the contact line or the particle, or both.

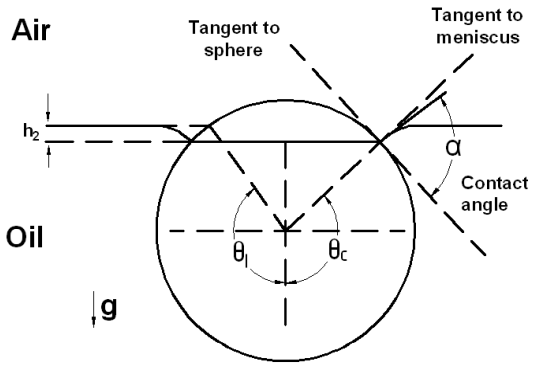

Figure 1.3 Schematic of a heavier than liquid hydrophilic (wetting) sphere of radius *a* hanging on the contact line at θ_c. The point of extension of the flat meniscus on the sphere determines the angle θ_1 and h_2 is defined as $h_2 = R\,(\cos\theta_c - \cos\theta_1)$. The angle α is fixed by the Young-Dupré law and θ_c by the force balance.

From Figure 1.3 it is easy to see that the vertical component of the capillary force (F_C) depends on the particle radius *R*, the surface tension coefficient γ, the filling angle θ_c and the contact angle α, and is given by

$$F_C = -2\pi R\gamma \sin\theta_c \sin(\theta_c + \alpha) \tag{1.3}$$

The above expression holds for all values of the contact angle, i.e., for both the hydrophobic and hydrophilic cases.

The buoyant weight of a particle can be written as

$$F_b = -g\rho_L R^3 f_b\left(\frac{\rho_a}{\rho_L}, \frac{\rho_p}{\rho_L}, \theta_c, \frac{h_2}{R}\right) \tag{1.4}$$

where g is the acceleration due to gravity, ρ_p is the particle density, ρ_a and ρ_L are the densities of the upper and lower fluids, θ_c and h_2 are defined in Figure 1.3, and f_b is a dimensionless function of $\frac{\rho_a}{\rho_L}$, $\frac{\rho_p}{\rho_L}$, θ_c and $\frac{h_2}{a}$.

As the particle radius decreases, the buoyant weight, which scales as R^3, becomes negligible in the sense that the vertical capillary force, which scales as R, needed to balance the buoyant weight is obtained by a negligibly small interfacial deformation (see Equations (1.3) and (1.4)).

As noted earlier, particles floating on a liquid surface can cluster under the action of lateral capillary forces. These forces arise when particles are heavier than the liquid below and thus float by deforming the interface. Specifically, when two heavy hydrophobic spheres are close to each other, the deformed interface around the spheres is not symmetric because the interface height between the spheres is lowered by the capillary force; on the other hand, lighter-than-water hydrophilic spheres will rise. In both of these cases, the lateral component of interfacial tension is attractive and the spheres tend to cluster. However, when one sphere is hydrophilic and the other one is hydrophobic, the lateral force at short range is repulsive and tight clusters cannot form.

1.2.1 Lateral Forces on a Particle

For the case where the meniscus slope and the particle size are small, in [18] the Laplace equation for the interface shape was solved using bipolar coordinates. This solution provides expressions for calculating the capillary meniscus force between two vertical disks, between two spheres partially immersed in a liquid layer, and between a vertical disk and a sphere. Specifically, in [5] it was shown that the lateral forces F_{lc} acting on two particles of radii R_1 and R_2 separated by the distance r are equal in magnitude and opposite in sign, and are given by

$$F_{lc} = -2\pi Q_1 Q_2 q K_1(qr)\left[1 + O(q^2 R_k^2)\right] \text{ when } L >> r_k. \tag{1.5}$$

Here $r_k = R_k \sin(\theta_c)$, k=1, 2 are the radii of the two contact lines (where the particle radius is assumed to be R), $Q_k = r_k \sin\psi_k$, where ψ_k is the interface slope with the horizontal plane at the point of contact, $q = \sqrt{(\rho_l - \rho_p)g/\gamma}$ is the inverse of the capillary length, and $K_1(x)$ is the modified Bessel function of the first order. Equation (1.5) is valid for particles much smaller than the capillary length.

$$F_{lc} = -\left(\frac{4}{3}\pi R^3 \rho_p g\, f_b\right)^2 \frac{1}{2\pi\gamma r}\,. \tag{1.6}$$

If the two particles are of the same type and size, and the distance between them is much larger than their radius, the lateral capillary force between them is given by the above simplified expression.

1.2.2 Vertical Force Balance

The vertical position of a particle floating within a fluid-liquid interface in equilibrium is determined by the condition that the sum of the forces acting on the particle in the direction normal to the interface is zero. If the particle density is larger than that of the lower liquid, equilibrium is possible only when the vertical component of the capillary force is large enough to balance its buoyant weight. The shape of the interface, in this case, is concave down and the net capillary force acts against gravity. The buoyant weight F_b of the particle is balanced by the capillary force $F_{c,}$ that is,

$$F_c + F_b = 0. \tag{1.7}$$

Using Equations (1.3-1.4), the above balance can be rewritten as

$$F_c = -2\pi\gamma R \sin\theta_c \sin(\theta_c + \alpha) = g\rho_L R^3 f_b\left(\frac{\rho_a}{\rho_L}, \frac{\rho_p}{\rho_L}, \theta_c, \frac{h_2}{R}\right). \tag{1.8}$$

In dimensionless form, the Equation 1.8 reads

$$2\pi \sin\theta_c \sin(\theta_c + \alpha) = -\mathrm{B}\ \ f_b(\frac{\rho_a}{\rho_L}, \frac{\rho_p}{\rho_L}, \theta_c, \frac{h_2}{R}). \tag{1.9}$$

Here B= $\rho_L R^2 g/\gamma$ is the Bond number.

The left hand side of Equation (1.9), and thus also its right hand side, lies in the range $-2\pi \le 2\pi \sin\theta_C \sin(\theta_C + \alpha) \le 2\pi$. Obviously, Equation (1.9) cannot be solved if B is too large, which may be the case when the sphere is too heavy or too large. As the particle radius *a* approaches zero, the Bond number also goes to zero, i.e. B= $\rho_L R^2 g/\gamma \to 0$. In this limit, in the absence of an electrostatic force, the right hand side of Equation (1.9) is zero and thus sin (α + θ_C) $\approx$ 0 or $\theta_C \approx \pi - \alpha$ (see Figure 1.3). This means that a small particle floats so that the interfacial deformation is insignificant. The vertical component of the interfacial force also decreases with decreasing radius, while remaining equal to the buoyant weight (which also decreases with the particle radius).

1.3 Dissertation Organization

The goal of this work is to study the physics of particle adsorption at a fluid-liquid interface, and the transient flow that results on the interface when a particle is adsorbed. The role of the parameters such as the properties of the particle and the fluids involved, the interfacial tension, and the contact angle in determining the motion of an adsorbed particle is also investigated. Specifically, it is shown that the motion of a particle in the

direction normal to the interface is inertia dominated and hence it has a characteristic frequency that can be excited by an external forcing.

Chapter 2 discusses the mechanism by which a particle is adsorbed. It is shown that the inertia of the particle plays an important role. Although the importance of inertia diminishes with decreasing particle size, on an air-water interface the inertia continues to be important even when the size is as small as a few nanometers. The linearized equation governing the motion of the particle is obtained to show that the motion is underdamped and that there is a characteristic frequency of oscillation. Chapter 2 also presents results for the frequency of oscillation when a single particle is adsorbed, and measurement of the characteristic frequency for adsorbed particles.

Chapters 3 and 4 describe the motion of a particle under an external forcing. Since the motion of a particle in the direction normal to the interface is similar to that of an underdamped system, the response is maximum for a characteristic frequency.

Chapter 5 describes the flow on the interface that is induced due to the adsorption a small number of particles.

Chapter 6 describes the Particle Image Velocimetry (PIV) technique designed to measure the fluid velocity induced due to the adsorption of a particle. The flow for a spherical particle is axisymmetric and so measured on the vertical plane passing through the center of the particle.

CHAPTER 2

ADSORPTION OF A PARTICLE ON A FLUID-LIQUID INTERFACE

It is shown that the inertia of a particle plays an important role in its motion in the direction normal to a fluid-liquid interface, and in determining its adsorption trajectory and orientation in the adsorbed state. Although the importance of inertia diminishes with decreasing particle size, on an air-water interface the inertia continues to be important even when the size is as small as a few nanometers. Furthermore, like an under-damped system, an adsorbed particle has characteristic linear and rotational frequencies that are excitable by excited by an external forcing.

2.1 Introduction

In recent years, there has been much interest in the absorbed state of colloidal particles at fluid-liquid interfaces, i.e., their positions and orientations within the interface, because of their importance in a range of applications [5-15]. In these studies, the stable state is determined by a static analysis of the forces and torques that act on the particle. The momentum equation governing the motion in the direction normal to the interface and the angular momentum equation governing the orientation, and the role of the particle inertia are not considered. However, since non-spherical particles can have multiple stable states, a static analysis, as noted in [41], is not sufficient for determining which of these states are more likely to be assumed by the particle. Furthermore [8] has recently shown that the motion of particles in the direction normal to the interface while being adsorbed gives rise to a secondary lateral flow on the interface that causes newly adsorbed particles

to disperse and those already present on the interface move away from the newly adsorbed ones (see Figure 1.1). This can influence the distribution and the state of particles on the interface.

This chapter shows that although the assumption that the inertia of small particles is negligible is justified in many problems involving colloidal particles because of their small mass, it may not be appropriate in the modeling of their adsorption at fluid-liquid interfaces. In fact, the motion of a particle in the direction normal to interface is similar to that of an under-damped system in that it has the characteristic linear and rotational frequencies that are excitable by an external forcing.

To show this, it is assumed that the inertia is negligible. Then, the velocity (V) of the particle is determined by a balance of the capillary and drag forces, which gives the velocity $V = \frac{\gamma_{12}}{\mu}$. Here γ_{12} is the interfacial tension between the upper and lower fluids and μ is the viscosity (which for simplicity is taken to be the larger of the upper or lower fluid's viscosity). The role of other forces, such as gravity, as discussed below, is negligible for small particles. The kinetic energy KE of the particle then becomes

$$KE = \frac{1}{2} m V^2 = \frac{2\pi\rho_p R^3}{3}\left(\frac{\gamma_{12}}{\mu}\right)^2 \tag{2.1}$$

where m is the particle mass, R is the particle radius and ρ_p is the particle density.

The adsorption energy W_a of a spherical particle, i.e., the decrease in the interfacial energy due to its adsorption, is given by [8]:

$$W_a = \pi R^2 \gamma_{12}(1+\cos\alpha)^2 \tag{2.2}$$

where α is the contact angle. Assuming that the contact angle is 90°, the ratio of the kinetic and adsorption energies becomes

$$\frac{KE}{W_a} = \frac{2\rho_p R\gamma_{12}}{3\mu^2} \tag{2.3}$$

Clearly, $\frac{KE}{W_a}$ must be *less* than one because the particle accelerates under the action of the capillary force and so its kinetic energy must be less than the interfacial work done on it; a value greater than one is physically erroneous. Furthermore, the inertia of the particle can be considered negligible only if its kinetic energy, a measure of the particle's inertia, is much smaller than the interfacial energy released during its adsorption, i.e., $\frac{KE}{W_a} << 1$.

Next this ratio for a neutrally buoyant particle at an air-water interface is evaluated, with parameters $\mu = 0.001$, $\rho_p = 1000$ kg/m^3 and $\gamma_{12} = 0.07$ N/m.

$$\frac{KE}{W_a} = \sim 10^8 R \tag{2.4}$$

Therefore, $\frac{KE}{W_a}$ = 1 for R = ~10 nm. Thus, the inertia of the particle can be considered negligible only when R is much smaller than 10 nm. Furthermore, R > ~10 nm results in $\frac{KE}{W_a}$ > 1, which is a consequence of the fact that the inertia of the particle was neglected. It is important to note that the continuum description being used may not be valid for such small particles.

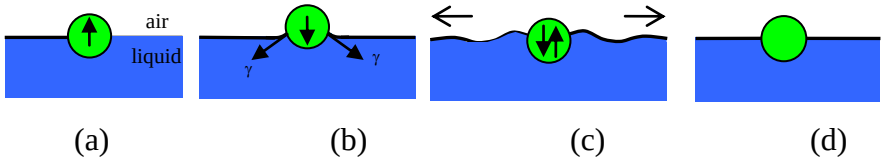

Figure 2.1. Vertical oscillation of a particle adsorbed at an air-liquid interface. The contact angle is assumed to be 90°, and so in equilibrium a small particle floats with its center at the undeformed interface. (a) The particle is pushed up from its equilibrium position in the interface. (b) The particle is pulled downwards by the interfacial force (γ). (c) The particle oscillates about the equilibrium height within the interface causing a radially outward secondary flow on the interface. (d) After oscillations subside, the particle assumes its equilibrium position.

2.2 Momentum Conservation

When a particle comes in contact with a fluid-liquid interface, or moves away from its equilibrium position in the interface, the component of the capillary force in the direction normal to the interface acts to bring it back to its equilibrium position (Figure 2.5). The motion of the particle is given by the governing equations for the two fluids and the momentum equation for the particle, which are coupled, along with the interface stress condition and a condition for the contact-line motion. This is a formidable problem which can be solved analytically only in simple situations [8, 35].

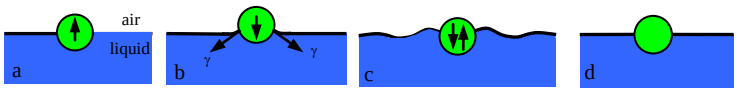

Figure 2.2 Vertical oscillation of a particle adsorbed at an air-liquid interface. The contact angle is assumed to be 90°, and so in equilibrium it floats with its center at the undeformed interface. (a) The particle is pushed up from its equilibrium position. (b) The particle is pulled downwards by the interfacial force (γ). (c) The particle oscillates about the equilibrium height. (d) After oscillations subside, the particle assumes its equilibrium position.

To quantify the role of various forces that act on a particle, consider the decoupled momentum equation in which the fluid forces that act on the particle are modeled [41, 42]. The forces that act on the particle are: the vertical capillary force (F_{st}), the buoyant weight (F_g), the Brownian force (F_B), and the viscous drag (F_D). The acceleration of a particle under the action of these forces can be written as:

$$m\frac{dV}{dt} = F_{st} + F_D + F_g + F_B \tag{2.5}$$

where m is the effective mass of the particle which includes the added mass contribution, and V is the velocity. The Brownian force which is included here for completeness is negligible compared to the capillary force, as will be discussed below, and therefore need not be considered.

For a spherical particle, $F_{st} = 2\pi R\gamma_{12}\sin(\theta_c)\sin(\theta_c + \alpha)$ (see Figure. 2.3) [8]. It is assumed that the drag force is given by: $F_D = 6\pi\mu RV f_{D,}$, where μ is the viscosity of the

lower liquid, and $f_{D.}$ is a coefficient which accounts for the fact that the particle is immersed in both upper and lower fluids. If $f_{D.}$=1, this expression reduces to Stokes law. Also, for simplicity, it is assumed that the added mass is one half of the mass of the fluid displaced [8]. Although this result is for a particle fully immersed in a fluid and not for a particle on the interface, it is not likely to change the qualitative nature of results. The angular velocity Ω of the particle is given by

$$\frac{d(\mathrm{I}_P\,\Omega)}{dt} = T_{st} + T_D + T_g\,, \tag{2.6}$$

where $\mathrm{I_P}$ is the moment of inertia of the particle, T_{st} is the torque due to the interfacial tension, T_D is the torque due to the viscous resistance, and T_g is the torque due to gravity. Here it is assumed that the shape of the particle is symmetric, e.g., a rod or an ellipsoid, and therefore only one component of the angular-momentum equation needs to be considered.

The torque on a spherical particle due to the interfacial tension is zero [44], and thus the rotational motion is not important for spherical particles. To illustrate the role of inertia in the rotational motion, consider a rod of length *L* and radius *R*, which in equilibrium floats on a liquid surface with its axis parallel to the surface (see Figure. 2.4). It is assumed that the contact angle is 90°, and that it floats such that one half of it is immersed in the liquid below. When the angle between the axis of the rod and the undeformed liquid surface is θ, an interfacial torque of $\gamma L^2\left(\frac{L}{6R}+2\frac{R}{L}\right)\sin\theta$ acts on the rod to bring it back to its equilibrium horizontal orientation. In addition, a frictional torque

$T_D = -\frac{\pi\mu L^3}{3}\ln\left(\frac{L}{2R}\right)\Omega$ acts on a rotating rod [45]. The moment of inertia of a rod about a direction normal to its axis is $\frac{mL^2}{12}$, where *m* is the mass of the rod.

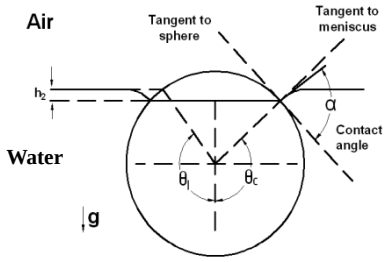

Figure 2.3 Schematic of a heavier-than-liquid hydrophilic (wetting) sphere hanging on the contact line at θ_c. The point of extension of the flat meniscus on the sphere determines the angle θ_1 and h_2.

2.2.1 Brownian Forces

The Brownian force in Equation (2.6) is negligible compared to the capillary force. To show this, note that the Brownian force cannot cause a particle to move away from its equilibrium position within the interface or de-adsorb when W_a is larger than *kT*, i.e., $\frac{W_a}{kT}$ $= \frac{\pi R^2 \gamma_{12}}{kT} > 1$. Here it is assumed that α is 90°. The same result can be obtained from the Peclet number defined to be the ratio of the capillary and Brownian forces: $Pe = \frac{RU}{D_B} = \frac{6\pi R^2 \gamma_{12}}{kT}$, where $U = \frac{\gamma_{12}}{\mu}$ is the characteristic velocity and $D_B = \frac{kT}{6\pi\mu R}$ is the Brownian diffusion coefficient [10]. This is the same condition except for a constant factor of 6 in the definition of the Peclet number. On an air-water interface, for *R*=1 μm, *Pe* = ~10^8;

and for R=10 nm, Pe = ~10^4. Therefore, for R > ~10 nm, the Brownian force is several orders of magnitude smaller than the capillary force (in the direction normal to the interface), and thus can be neglected.

2.2.2 Governing Dimensionless Parameters

Assuming that the characteristic velocity, length and time are $U=\gamma_{12}/\mu$, R, and R/U, respectively, Equation (2.5) can be nondimensionalized to give [8]

$$\mathrm{We}\, m' \frac{\rho_p}{\rho}\frac{\mathrm{d}V'}{\mathrm{d}t'} = \sin(\theta_c)\sin(\theta_c+\alpha) + 3V' f_D + \frac{2}{3}B\frac{\rho_p-\rho_c}{\rho} f_b\left(\frac{\rho_a}{\rho},\frac{\rho_p}{\rho},\theta_c,\frac{h_2}{R}\right) \tag{2.7}$$

Here the primed variables are dimensionless. f_b is the dimensionless buoyancy which is O(1) but depends on the profile of the deformed interface. θ_c and h_2 are defined in Figure. 2. μ and μ_a are the viscosities of the lower and upper fluids, and ρ and ρ_a are their densities, ρ_c is the effective density of the volume displaced by the particle, and ρ_p is the particle density. The dimensionless parameters in the above equation are: the Weber number $We = \frac{2}{3}\frac{\rho R\gamma_{12}}{\mu^2}$, the Bond number $B = \rho R^2 g/\gamma_{12}$, the density ratio $\frac{\rho_p}{\rho}$, and the contact angle α. The Weber number is the ratio of fluid's inertia and surface tension, and the Bond number is the ratio of gravity and surface tension forces. As the characteristic velocity is the capillary velocity, the capillary number is unity [18]. Thus, the Reynolds number (*Re*), which is product of *We* and capillary number, becomes the same as *We*, i.e., *Re*=*We*.

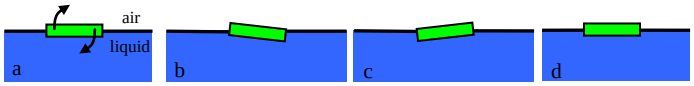

Figure 2.4 Rotational oscillation of a cylindrical rod adsorbed at an air-liquid interface. The contact angle is assumed to be 90°, and so in equilibrium the rod floats with its center at the undeformed interface and axis parallel to the interface. (a) The rod is rotated clockwise from its equilibrium orientation. (b) The rod rotates in the direction of the torque, but is pulled back by the interfacial torque towards its equilibrium orientation. (c) The rod oscillates about the equilibrium orientation. (d) After the oscillations subside, the rod assumes equilibrium orientation.

Similarly, assuming that the characteristic angular velocity, length and time are $\frac{\gamma_{12}}{\mu L}$, L, and $\frac{\mu L}{\gamma_{12}}$, respectively, Equation (2.6) can nondimensionalized to give

$$\frac{\pi}{8}\frac{R}{L}\frac{\rho_p}{\rho}We\frac{d\Omega'}{dt'} = \sin\theta\left(\frac{L}{6R}+2\frac{R}{L}\right) - \frac{\pi}{3}\ln\left(\frac{L}{2R}\right)\Omega' - \frac{1}{6}B\frac{L}{R}\frac{\rho_p-\rho_c}{\rho}\sin\alpha\,\tan\theta\cos\theta \tag{2.8}$$

The dimensionless parameters in this equation are $\frac{R}{L}$, and those in Equation 2.7 are We, B, $\frac{\rho_p}{\rho}$, and α.

To illustrate these results, consider the case of a particle on an air-water interface, assuming the parameters to have the values: $\mu = 0.001$ Pa.s, $\rho = \rho_p = 1000$ kg/m^3, $\frac{\rho_p - \rho_c}{\rho} = 0.1$ and $\gamma_{12} = 0.07$ N/m, and $\mu_a = \rho_a = 0$, m'=1.5, f_d=0.5 and f_b=1. Therefore, for an air-water interface: $We = \sim 10^8 R$ and $B = \sim 10^5 \mathrm{R}^2$.

The role of particle inertia becomes negligible only when We <<1 or R is much smaller than 10 nm. The influence of gravity on an air-water interface becomes negligible when B is small or R < ~ 1 mm in the sense that such small particles float so that the interfacial deformation is negligible [8, 24]. However, even a negligibly-small deformation of the interface gives rise to attractive lateral capillary forces which, even though small, cause floating particles to cluster. This happens because a particle floating on a liquid surface is free to move laterally. The only resistance to its lateral motion is the hydrodynamic drag which can slow its motion but cannot stop it.

Therefore, only very-small particles, for which lateral capillary forces are smaller than Brownian forces, do not cluster. For example, on an air-water interface, lateral capillary forces become smaller than Brownian forces when R < ~ 10 μm, and so micron and smaller sized particles undergo Brownian motion on the interface and do not cluster [24-16]. Meanwhile, the capillary force which acts vertically to pull the particle back toward its equilibrium position in the interface remains much stronger than the Brownian force even for nanoparticles.

2.3 Vertical Oscillation of a Sphere

The experiments and direct numerical simulations show that when a particle being adsorbed reaches the equilibrium height for the first time, its velocity is non-zero, and so it continues to move downwards [16]. However, when the particle center moves below the equilibrium height, the vertical capillary force changes direction and acts upwards to bring the particle back to the equilibrium height. This suggests that the motion of the

particle in the direction normal to the interface is inertia dominated. This can be also seen by linearizing Equation. (2.7) about the particle's equilibrium position.

The right-hand side of Equation (2.7) was approximated in [8] by assuming that the contact angle is equal to its equilibrium value, the drag force is given by the Stokes formula, and the buoyancy force depends on the particle's vertical position, to obtain

$$m\frac{\mathrm{d}V}{\mathrm{d}t} = -2\pi(R\sin\theta_c)\gamma\sin(\theta_c+\alpha) - 6\pi \mathrm{R}\mu V\zeta(s) + \mathrm{Q}(\rho_\mathrm{p} - \rho_\mathrm{c})\mathrm{g}\ . \tag{2.9}$$

Here $\zeta(s)$ is a parameter that accounts for the dependence of the drag on the fraction s of the particle that is immersed in the lower and upper fluids and on the viscosities of the fluids, Q is the particle volume, ρ_c is the effective fluid density which changes with s while the particle moves in the direction normal to the interface, and ρ_p is the particle density.

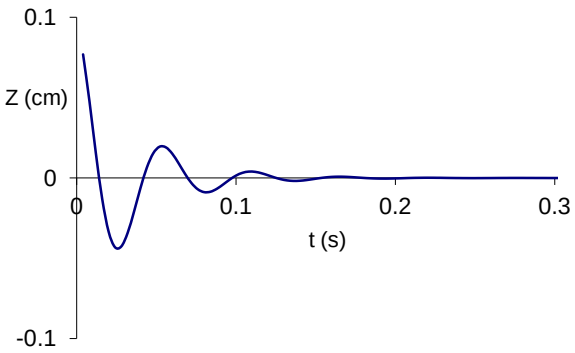

Figure 2.5 The z-coordinate of the particle center obtained numerically by solving equation. (4) is shown as a function of time. The particle oscillates about the equilibrium position (z=0) before coming to rest. The amplitude of oscillations decreases with increasing time. The parameters are the same as in Figure 2.3 [8].

Equation (2.7) can be linearized about the particle's equilibrium position to show that it is equivalent to a mass-spring-dashpot system [26]. Assuming that $\alpha = \frac{\pi}{2}$, $\theta_c = \frac{\pi}{2}$ and $\zeta(s) = 1/2$, after linearization, Equation (2.10) is obtained.

$$\frac{4}{3}R^3\rho_p\frac{\mathrm{d}^2Z}{\mathrm{d}t^2} + 3\mathrm{R}\mu\frac{\mathrm{dZ}}{\mathrm{d}t} + 2\gamma Z + R^2\left(\rho_\mathrm{p} - \rho_\mathrm{c}\right)\mathrm{g}\,\mathrm{Z} = 0 \tag{2.10}$$

where Z is the particle's position. The solution of this ordinary differential equation can be written as:

$$Z = Z_0 e^{kt} \tag{2.11}$$

where $k = \frac{-3R\mu \pm \sqrt{D}}{\frac{8}{3}R^3\rho_p}$ and $D = 9R^2\mu^2 - \frac{16}{3}R^3\rho_p\left(2\gamma + R^2\left(\rho_p - \rho_c\right)g\right)$. The nature of the solution depends on the sign of the discriminant *D*. If the sign is positive, then *k* is real and negative for both of the roots. In this case, the solution decays exponentially with time to zero. This is expected to be the case when the fluid viscosity is sufficiently large. If the sign of *D* is negative, then *k* is complex and the solution is oscillatory. In this case, the frequency of the oscillation is given by

$$\omega = \frac{3\sqrt{-9R^2\mu^2 + \frac{16}{3}R^3\rho_p\left(2\gamma + R^2\left(\rho_p - \rho_c\right)g\right)}}{16\pi R^3\rho_p} \tag{2.12}$$

The real parts of both roots are negative and so both of the solutions decay exponentially to zero. The time constant τ of the solution, i.e., the time taken by the solution to decay by a factor of e^{-1}, is given by

$$\tau = \frac{8R^2\rho_p}{9\mu} \tag{2.13}$$

It is clear that time constant τ decreases with decreasing particle size and with increasing viscosity. Therefore, the vertical oscillations of a trapped particle decay faster when the radius is smaller and the viscosity is larger. Notice that as *R* becomes small**,** there is a critical value of *R* for which *D* becomes positive. The dimensionless frequency of oscillation ω' can be written as

$$\omega' = \omega \frac{R\mu}{\gamma_{12}} = \frac{3}{8\pi We} \frac{\rho}{\rho_P} \sqrt{-1 + \frac{8}{9} We \frac{\rho_P}{\rho} \left(2 + B \left(\frac{\rho_p - \rho_c}{\rho} \right) \right)} \qquad (2.14)$$

The frequency ω increases with decreasing R (or We). For an air-water interface, the frequency of oscillation (ω) in Hz is plotted as a function of the particle radius in Figure 2.6. The frequency increases with decreasing particle radius. For R=1 mm, ω = 51.6 Hz; for R=10 μm, ω =5.2x10^4 Hz; and for R=100 nm, ω = 5.1x10^7 Hz.

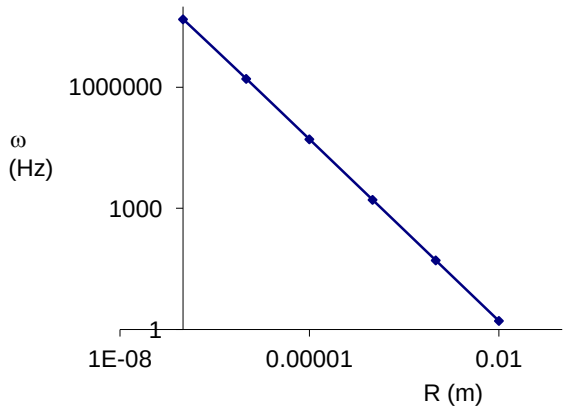

Figure 2.6. The frequency (ω) of oscillation of the solution given by Equation (2.14) is plotted as a function of the particle radius. The parameter values were assumed to be: $\mu = 0.001$ Pa.s, $\rho_p = 1000.0$ kg/m^3, $\rho_p - \rho_c = 0.1$ kg/m^3 and $\gamma_{12} = 0.07$ N/m.

2.3.1 Vertical Oscillation of a Particle During Adsorption

Above analysis and direct numerical simulations show that while a particle is being trapped on the surface of a mobile liquid, it oscillates about their equilibrium positions before reaching a state of rest, and that this results in a radially-outward flow on the interface away from the particle which causes tracer and other particles on the interface to move away. To investigate these oscillations, the video recordings of the motion of

particles after they came in contact with the interface were analyzed. The particle size was varied between approximately 5 μm and 4 mm. The behavior was investigated for the air-water, oil-water and decane-water interfaces.

The motion of a 2 mm spherical plastic bead from the time it came in contact with the decane-water interface is shown in Figure 2.7. The bead released in the upper liquid slowly sedimented to the decane-water interface, and once it came in contact with the interface, it was pulled downwards by the vertical capillary force. The bead continued to move downward even after reaching the equilibrium height. However, when this happened the vertical capillary force reversed its direction and thus after travelling some additional distance, the direction of bead's motion also reversed. The bead oscillated three times about its equilibrium position before its motion became indiscernible. Since the bead overshoots and oscillates about the equilibrium position before stopping, it can be concluded that its motion is inertia-dominated and similar to that of an underdamped mass-spring-dashpot system. The motion of the bead also caused ring-shaped interfacial waves that moved away from the bead and slowly dissipated. Notice that the frequency of oscillation was 20 Hz or larger, and therefore a high speed camera was needed to see and analyze the motion.

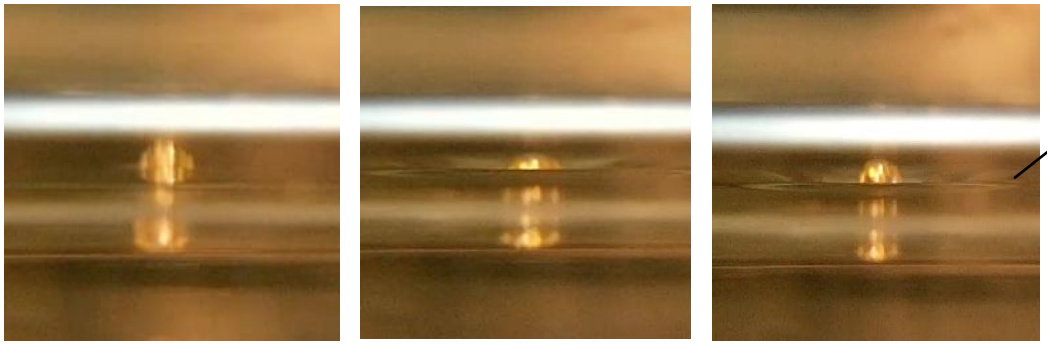

t = 0.0066 s (going down) t = 0.01 s (going down) t = 0.0633 s (coming up)

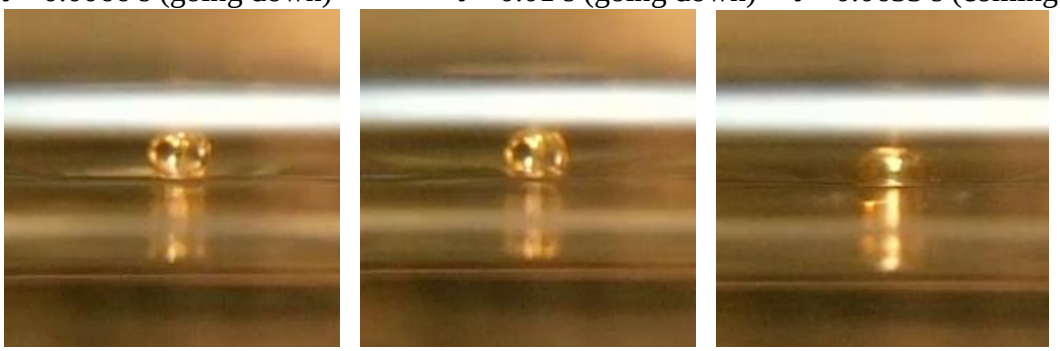

t= 0.0866 s (highest position) t = 0.09 s (again going down) t = 0.1133 s (going down)

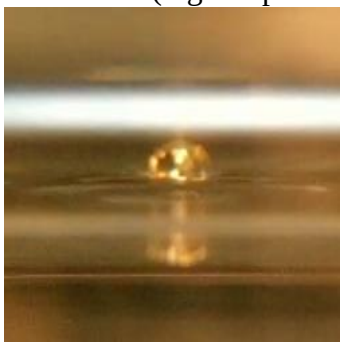

t = 0.126 s (coming up)

Figure 2.7 Trapping of a spherical plastic bead of 2 mm diameter on the decane-water interface. The bead oscillated about its equilibrium position before its motion stopped. The sequence shows the phenomenon from the time the bead touched the interface to the time it reached the equilibrium position.

The photographs shown in Figures 2.7 were taken from high-speed movies of particles undergoing adsorption at the fluid-liquid interfaces. These movies were also analyzed frame-by-frame to obtain the dimensionless distance of the center of particles (Z/*R*) from the undeformed interface as a function of time. The dependence of the frequency of oscillation of glass particles on the air-water and decane-water interfaces on

their diameter was also investigated. These results are shown in Figure 2.7. For both interfaces the frequency increased with decreasing particle size. The frequency of oscillation was larger on the air-water interface than of the same particle on the decane-water interface. These results are in agreement with analysis presented in Equation 2.14. It is noteworthy that Equation 2.14 contains only the fluid and particle properties, and that there are no adjustable parameters.

2.4 Rotational Oscillation of a Rod

Similarly, Equation 2.2 can be linearized about the equilibrium orientation to show that the rotational behavior of a rod when disturbed from equilibrium orientation depends on the sign of

$$D_r = \left(\frac{\pi}{3}\ln\left(\frac{L}{2R}\right)\right)^2 \left(1 - \frac{9}{2\pi}\frac{We}{\left(\ln\left(\frac{L}{2R}\right)\right)^2}\frac{\rho_p}{\rho}\left(\frac{1}{2}\frac{R}{L} + 2\left(\frac{R}{L}\right)^2 - \frac{4}{3}\frac{\rho_p - \rho_c}{\rho}B\right)\right) \tag{2.15}$$

The contact angle has been assumed to be 90°. The rod undergoes underdamped rotational oscillations about the equilibrium orientation when $D_r < 0$. The dimensionless rotational frequency ω_r' of the rod for $D_r < 0$ is given by:

$$\omega_r^{'} = \omega_r \frac{\mu L}{\gamma_{12}} = \frac{4}{3}\frac{L}{R}\ln\left(\frac{L}{2R}\right)\frac{1}{We}\frac{\rho}{\rho_p}\sqrt{\left(-1+\frac{9}{2\pi}\frac{We}{\left(\ln\left(\frac{L}{2R}\right)\right)^2}\frac{\rho_p}{\rho}\left(\frac{1}{6}+2\left(\frac{R}{L}\right)^2-\frac{1}{6}\frac{\rho_p - \rho_c}{\rho}B\right)\right)} \tag{2.16}$$

Note that the rotational frequency ω_r depends on *We, B,* the density ratios and the aspect ratio $\frac{L}{R}$, and that it is different from the characteristic frequency with which a rod oscillates vertically. The frequency ω_r increases with decreasing *R* (or *We*), and decreases with increasing aspect ratio $\frac{L}{R}$. For example, for an air-water interface for $\frac{L}{R}$ = 4, $\frac{\rho_p}{\rho}$ = 1, for *R* = 1 mm, ω_r = 317.9 Hz; for *R*=10 μm, ω_r = 3.2x10^5 Hz; and for *R* = 100 nm, ω_r = 2.7x10^8 Hz. For $\frac{L}{R}$ = 8, $\frac{\rho_p}{\rho}$ = 1, for *R* = 1 mm, ω_r = 261.4 Hz; for *R*=10 μm, ω_r = 2.6x10^5 Hz; and for *R* = 1 μm, ω_r = 7.6 x10^6 Hz. For this larger value of the aspect ratio, when *R* is O(100 nm) the rotational motion of the rod becomes overdamped.

2.5 Particle Velocity During Adsorption

Equation (2.2) can be integrated to obtain the particle velocity when it passes through its equilibrium position for the first time [8].

$$V = \frac{-\frac{9}{4}\mu + \sqrt{\frac{81}{16}\mu^2 + 4R\rho_p\left(\frac{3}{2}\gamma + 2R^2\left(\rho_p - \rho\right)g\right)}}{2R\rho_p} \tag{2.17}$$

In obtaining above equation, it assumed that the contact angle is 90° and that in equilibrium the center of the particle is at the undeformed interface. The above equation implies that the maximum velocity attained by a particle increases with decreasing particle radius (see Figure 2.3). For example, a particle of diameter 200 μm (which is roughly the size of a sand particle) can accelerate to a velocity of ~1 m/s at the water surface, and a particle of diameter 10 nm, which is roughly the size of a virus or a protein molecule, to a velocity of ~40 m/s. In the limit of R approaching zero, the velocity is given by

$$V = \frac{2\gamma}{3\mu}. \tag{2.18}$$

This is the maximum velocity that can be attained by a particle under the action of the vertical capillary force, which for the air-water interface, is 46.7 m/s.

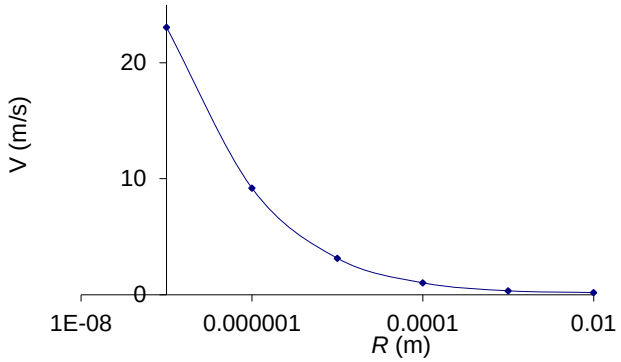

Figure 2.8 The velocity of a spherical particle normal to the interface given by Equation 2.17 is plotted as a function of the particle radius. The parameter values are the same as in Figure 2.2.

2.6 Conclusion

In conclusion, it is shown that the behavior of particles adsorbed at fluid-liquid interfaces in the direction normal to the interface is different from that in the lateral direction to the interface. This is a consequence of the fact that particles are free to move laterally on the interface just like when they are fully immersed in a fluid, but in the direction normal to the interface the capillary force keeps the particle at their stable positions in the interface. Consequently, although inertia can be usually neglected for a colloidal particle fully immersed in a fluid, this may not be case for a particle trapped at a fluid-liquid interface even when its size is as small as a few nanometers. Furthermore, for an adsorbed particle there are characteristic linear and rotational frequencies that can be excited by an external forcing. This latter behavior of particles is similar to that of an under-damped mass-spring-dashpot system.

CHAPTER 3

FORCED OSCILLATIONS OF PARTICLES ON FLUID-LIQUID INTERFACES

To study the parameters pertinent to the forced oscillation of the particle it was necessary to consider the periodic force acting in the plane normal to the interface. Adding an external force changes the system to a forced overdamped mass-spring-dashpot system. This section explains how this force was used to find the resonance frequency of the system.

3.1 Forcing Frequency

In order to study the particle under forced oscillations, an experiment was designed with an oscillatory magnetic force acting on the particle. The magnetic force was generated using an electromagnet that was subjected to an oscillatory voltage. The current flowing though the electromagnet was proportional to the applied voltage. The particle was ferromagnetic and the magnetic field was varied in both strength and forcing frequency ω to change the force acting on the particle.

When the floating particle is subjected to an externally-applied oscillatory magnetic force, $F_m \sin(\omega t)$ in the perpendicular direction to the interface its motion is governed by the following equation:

$$m\frac{\mathrm{d}V}{\mathrm{d}t} = \mathrm{F_{st}} + \mathrm{F_D} + \mathrm{F_g} + F_m \sin(\omega t) \tag{3.1}$$

Here the term $F_m \sin(\omega t)$ is the external force acting on the particle due to the electromagnet mounted above the particle. The linearized version of the above equation is given by,

$$\frac{4}{3} R^3 \rho_p \pi \frac{d^2 Z}{dt^2} + 3R\mu\pi \frac{dZ}{dt} + \left(2\gamma_{12} + R^2(\rho_p - \rho_c)g\right)\pi Z = F_m \sin(\omega t) \tag{3.2}$$

Now to compute the resonance frequency the equation is written as a differential equation of the form given by Equation 3.3.

$$\frac{d^2 Z}{dt^2} + 2\xi\omega_0 \frac{dZ}{dt} + \omega_0^2 Z = \frac{F_m}{m} \sin(\omega t) \tag{3.3}$$

Here ω_0 is the undamped natural frequency and ξ is the damping ratio of the system which are given by,

$$\omega_0^2 = \frac{3}{4} \frac{\left(2\gamma_{12} + R^2(\rho_p - \rho_c)g\right)}{4R^3 \rho_p} \tag{3.4}$$

$$2\xi\omega_0 = \frac{9}{4} \frac{\mu}{R^2 \rho_p} \tag{3.5}$$

The inertia m of the particle which depends on the radius as well as density of the particle and is given by

$$m = \frac{4}{3} R^3 \rho_p \pi \tag{3.6}$$

The steady-state solution of the above Equation is proportional to the driving force $F_m \sin(\omega t)$ and phase change of ϕ is given by,

$$x(t) = \frac{F_m}{m Z_m \omega} \sin(\omega t + \phi) \tag{3.7}$$

Here ϕ is the difference in phase between driving and driven frequencies and Z_m is the absolute value of the linear response function, and they are defined as

$$\phi = \arctan\left[\frac{\frac{9}{4}\left(\frac{\mu\omega}{R^2 \rho_p} \right)}{\omega^2 - \frac{3}{4} \frac{\left(2\gamma_{12} + R^2\left(\rho_{\mathrm{p}} - \rho_{\mathrm{c}}\right)\mathrm{g}\right)}{4R^3 \rho_{\mathrm{p}}}} \right] \tag{3.8}$$

$$Z_m = \sqrt{\left(\left(\frac{9}{4} \frac{\mu}{R^2 \rho_p} \right)^2 + \frac{1}{\omega^2} \left(\frac{3}{4} \frac{\left(2\gamma_{12} + R^2\left(\rho_{\mathrm{p}} - \rho_{\mathrm{c}}\right)\mathrm{g}\right)}{R^3 \rho_{\mathrm{p}}} - \omega^2 \right)^2 \right)} \tag{3.9}$$

The general solution comprises of the transient solution from Equation 3.3 and the steady state solution from Equation 3.7 and is given by

$$Z = Z_0 e^{kt} + \frac{F_m}{mZ_m\omega}\sin(\omega t + \phi) \tag{3.10}$$

The steady-state solution contains a forcing function and the transient solution is independent of the forcing function. For the naturally-damped case as $t \to \infty$ the amplitude of oscillations will become zero. However, with forced oscillations the amplitudes will be non-zero due to the added value from the steady state solution. In the case of forced oscillation of an underdamped system, it should be possible to obtain continuous oscillations. There is no exponential term in the steady-state solution so the maximum amplitude will be constant if the driving frequency ω is not changed. During the experiments, enough time was allowed after changing the frequency so that the transient part of the solution is zero

The resonance frequency is given by

$$\omega_\tau = \sqrt{\left(\frac{3}{4}\frac{\left(2\gamma_{12} + R^2\left(\rho_{\mathrm{p}} - \rho_{\mathrm{c}}\right)\mathrm{g}\right)}{R^3\rho_{\mathrm{p}}}\right) - \frac{1}{2}\left(\frac{9}{4}\frac{\mu}{R^2\rho_p}\right)^2} \tag{3.11}$$

It is expected that when the forcing frequency ω is close to ω_τ resonance will occur. This will result in substantially-larger amplitudes than the amplitudes at nearby frequencies which will be discussed in the results section. An experiment was designed to study the motion of a particle under forced oscillation, and the setup and results of the experiment are discussed in Chapter 4

CHAPTER 4

EXPERIMENTAL SETUP AND RESULTS FOR FORCED OSCILLATIONS

It is shown in Chapter 2 and Chapter 3 that as once a particle touches the interface it is pulled inwards to its equilibrium position by the vertical component of capillary force. The motion of the particle is dominated by inertia and it overshoots the equilibrium. The viscous drag causes the particle to slow down, but its magnitude is not large enough to stop the particle completely and consequently the momentum of particle carries it below the equilibrium height. As the particle moves below its equilibrium height, the capillary force reverses its direction and acts in the same direction as the drag. Hence, after moving down some additional distance, the particle reverses its direction, leading to several oscillations before the particle comes to rest. This behavior of the particle is similar to that of under-damped mass-spring-dashpot systems. The purpose of this experiment was to include a forcing function so that the system becomes a forced under-damped mass-spring-dashpot system. This addition of force enables us to determine the natural frequency of the system as shown by Equation 3.11.

To study the particle under forced oscillations, an experiment was designed with oscillatory magnetic force acting on the particle. The magnetic force was generated using an electromagnet that was subjected to an oscillatory voltage. The current flowing though the electromagnet was proportional to the applied voltage. The particle was ferromagnetic and the magnetic field was varied to change the force acting on the particle with ω as the forcing frequency. As the forcing frequency is varied the particle oscillates at different amplitudes. Maximum amplitude is observed when the frequency of oscillation of the

particle is same as the applied forcing frequency. This chapter explains how this external force was used to find the resonance frequency of the system.

4.1 Experimental Setup

To apply the magnetic field, an electromagnet was connected to a function generator via an amplifier and diode circuit. The function generator allowed us to change the wave form and the frequency of the applied electric signal. The amplifier was used to adjust the strength of the electric field. Diode was used in the circuit between the amplifier and the magnet such that the electro magnet will be magnetized only for a half cycle i.e. the particle will experience force in only one direction. Since the particle floating on the interface is ferromagnetic it experiences periodic force in the upwards direction.

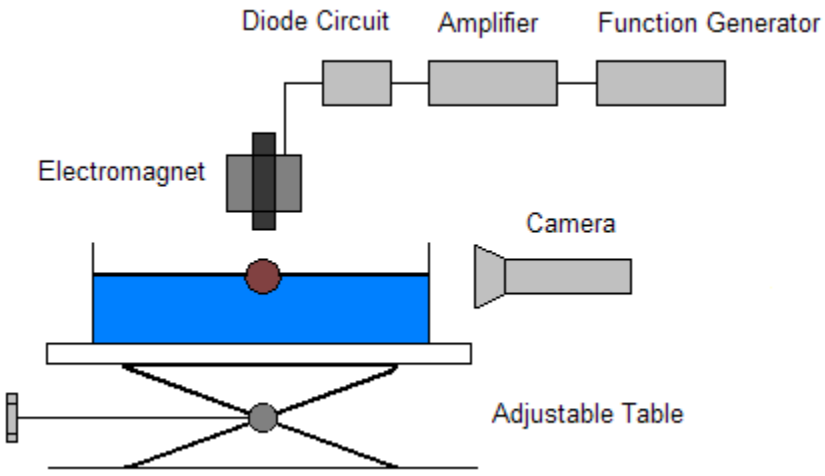

Figure 4.1 Schematic of the experimental setup used to study the forced oscillations of a steel bead floating on a liquid surface. An oscillating voltage from a function generator was amplified and then applied to an electromagnet mounted directly above the interface to produce an oscillating magnetic field. The bead was subjected to this oscillating magnetic force in the direction normal to the interface. The vertical oscillations of the bead were recorded using a high speed camera.

A Petri dish was placed below the electromagnet on an adjustable table such that the height of the Petri dish relative to the electromagnet could be varied. This enabled us to change the intensity of the magnetic field by changing the electric field strength or changing the distance between particle and the magnet. Deionized (DI) water from Millipore was used throughout the experiment to avoid any contaminants. Any impurities might act as a surfactant in the liquid resulting in reduced surface tension. The reduced surface tension would affect the frequency of oscillations as the vertical capillary force brings the particle towards equilibrium. The Petri dish was rinsed with DI water before every use. Since the surface tension of the liquids involved was very important, the experiment was performed several times to ensure repeatability. The experiment was performed with two different combinations of interfaces air - water and Corn oil - water. The interfacial tension between air-water is 72.4 mN/m, and corn oil-water is 33.2 mN/m. The viscosity of water is 1.0 cP and that of corn oil is 65.0 cP.

A high speed camera was mounted on the side to ensure that the oscillations of the particle could be studied and analyzed. The videos were recorded with 600 fps and then analyzed frame by frame to compute amplitude as a function of frequency. To measure the amplitude the particle’s highest point to the lowest point is measured during one half cycle. This measurement is done over 5 complete cycles and an average is used to avoid errors.

4.2 Description of the Experiment

To conduct the experiment a ferromagnetic spherical particle was dropped in the Petri dish filled with DI water using a clean forceps. In case of oil-water interface, the particle was dropped on the DI water surface and then the corn oil was poured gently. Once the particle was dropped, the electromagnet was mounted on the top.

To study the full dynamics of the system, both field strength and frequency of oscillations was varied and corresponding amplitude was computed. Periodic magnetic field was applied to the particle from the top such that the particle is forced out of its equilibrium. The strength of the magnetic field was varied by changing the distance between the electro magnet and the particle. For every distance i.e. field strength the frequency was varied from 8 Hz to 80Hz.

A square wave was used as input with diodes in the circuit such that the magnet will be magnetized only for a half cycle of the square wave. Square wave was selected as it gives larger values of force compared to the sinusoidal wave. Thus a periodic force in upwards direction is observed by the particle floating on the interface. Here the frequency of the applied magnetic force on the particle will be same as the frequency of electric field applied. The particle travels downwards towards equilibrium as soon as the magnetic force is removed. It overshoots the equilibrium and travels back up towards equilibrium. Depending on the applied frequency, the magnetic field turns back on which pulls the particle upwards. This leads to continuous oscillation of the particle on the fluid-liquid interface. Square wave gives larger values of force compared to the sinusoidal wave. Thus, by varying the electric frequency ω_i using the function generator the forcing frequency ω could be varied.

To understand the dynamics of the system, multiple sizes of spherical steel particles which were ferromagnetic in nature were required for this experiment. Various sizes starting from 500 μm to 2 mm were tested for these experiments. As explained in Chapter 2, Equation 2.12 the frequency of the particle depends on the size apart from the physical properties. Solid steel spheres of size 500, 632 and 700 μm were used in the experiments.

Since steel particles larger than 1 mm would sink in water, plastic beads with steel core were used as an alternative. A plastic spherical bead 2 mm in diameter with a hole in the center was used as base material. A cylindrical steel wire was cut to the length of diameter of the sphere and grounded on the edges to keep the ends flat. This wire is then placed inside the sphere and glued in place. It is important to note that the process of making the beads is not perfect. If there is any misalignment between the beads center of gravity and the steel cylinder's center of gravity, the bead will not oscillate vertically, but will wiggle around instead. Only beads which were oscillating vertically along their axis were used and the rest were discarded.

4.3 Results

As discussed before, when a particle is dropped on a fluid-liquid interface, it oscillates about its equilibrium before coming to rest. If a periodic force normal to the interface is applied to the particle, the particle will oscillate continuously. By varying the applied frequency ω, the resonant frequency ω_τ of the system can be found out. At resonant frequency ω_τ, the particle's amplitude of oscillations would be larger than at adjoining frequencies. Since the frequency of electric signal ω_i has linear relationship to the

frequency of oscillations ω, the value of ω_i is varied using the function generator. The function generator is then connected to the amplifier which supplies current to the electromagnet via a diode. The particle was floating on the fluid interface below the core of the electromagnet.

To compute the amplitude of the oscillation of the particle at various frequencies and strength, both the strength of the magnetic field and the frequencies were varied. For a fixed distance between the electromagnet and the particle, the frequency of oscillations was varied between 8Hz to 80Hz by using the function generator. For every frequency the amplitude was computed. Then the strength of the magnetic field was changed by changing the distance between the electromagnet core and the particle. This was repeated multiple times and Figure 4.2 was computed, where amplitude as function of frequency can be seen for various strengths of magnetic field.

4.3.1 Particle on air-Water Interface

When the upward force on the particle is removed, the particle is pulled towards the interface under the action of the vertical capillary forces. Since the system is underdamped, the particle over shoots the equilibrium. Now it is lower than the equilibrium and the capillary forces pulls it back upwards. Depending on the natural frequency of the particle ω_0 and that of the forcing function ω, the particle has a phase lag ϕ. When the forcing frequency ω matches the natural frequency ω_0 of the particle, the particle resonates and maximum amplitude is observed. This can be seen from the above Figure 4.2, where the particle resonates at around 20 Hz.

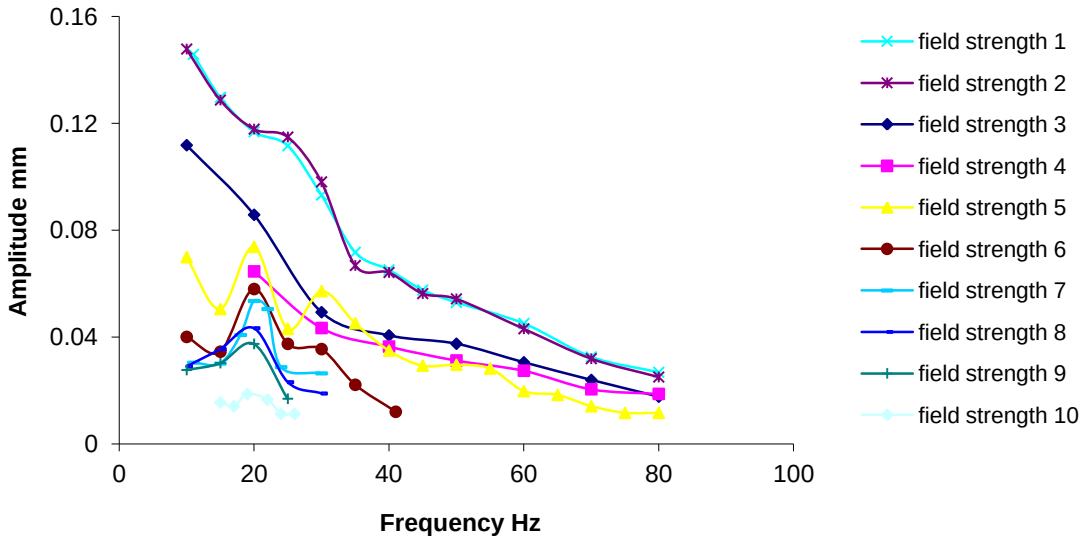

Figure 4.2 Plot of amplitude of oscillation vs. frequency for 632 µm particle on air water interface.

The Figure 4.2 describes variation of amplitude as a function of frequency where the force from the magnetic field was varied by changing the distance between the magnet and the particle. It can be seen from the Figure 4.2 for field strength 6, that the amplitude at 20 Hz is around 14% larger than the amplitude at 15 or 25 Hz. At this frequency, the particle's natural frequency ω_0 matches that of the applied frequency ω which leads to resonance. Due to the damping characteristics of the water, the amplitude cannot rise to higher values.

It can also be seen that this phenomenon is only valid for smaller amplitudes; at larger amplitudes the particle's amplitude reduces as the frequency increases irrespective of its natural frequency. This may be due to change in dynamics governing the system in the form of increased velocity of the particle. When the magnetic force is large, the amplitude decays exponentially as the frequency is increased from 10 Hz to 80 Hz.

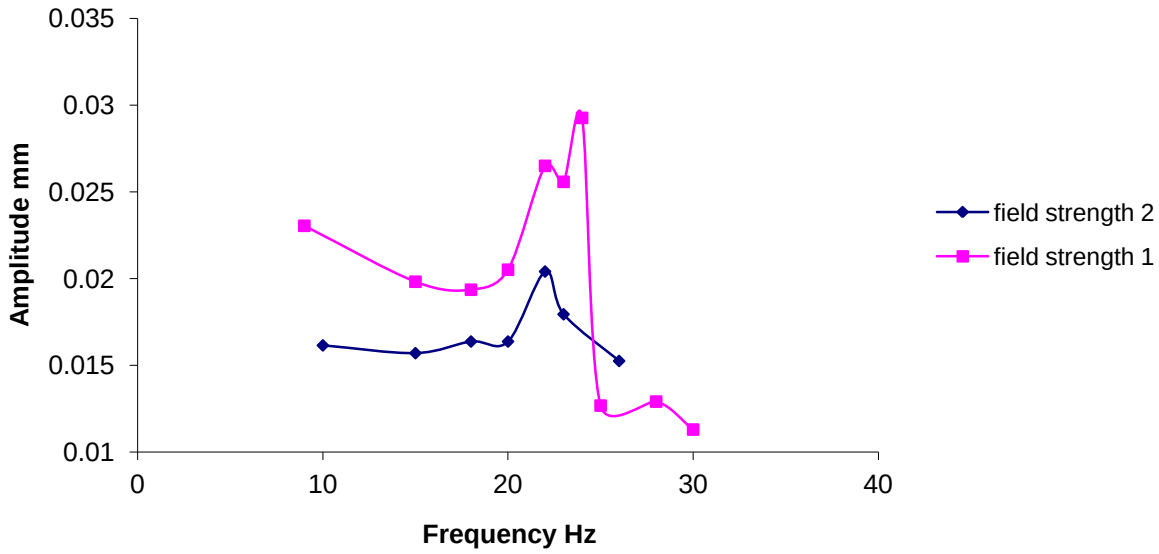

Figure 4.3 Plot of amplitude of oscillation vs. frequency for 500 µm particle on air water interface.

The same experiment was performed for a 500 µm spherical ferromagnetic particle. The particle exhibits behavior similar to 632 µm particle as seen in Figure 4.3. The frequency was varied from 10 to 30 Hz. This shows the particle exhibits resonance behavior at specific frequency. When the applied frequency was 24 Hz, the particle showed resonance with maximum amplitude of 0.03 mm corresponding to field strength 2 whereas the amplitude at 20 Hz was 0.02 mm and at 25 Hz was 0.15 mm. The resonant frequency of a 500 µm particle is significantly higher than that of 2 mm particle.

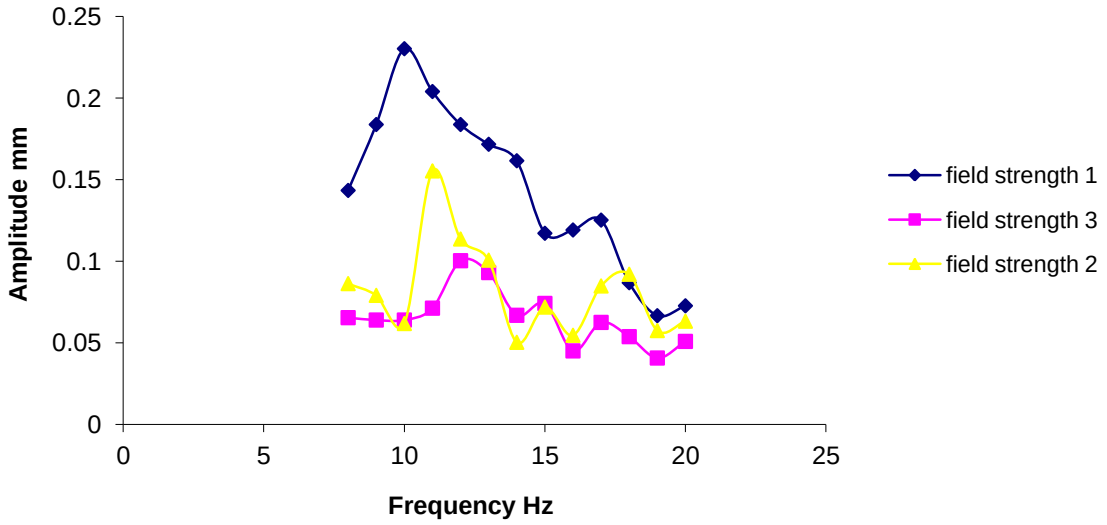

Figure 4.4 Plot of amplitude of oscillation vs. frequency for 2 mm bead on air water interface.

Since steel particles larger than 1 mm would sink in water, plastic particles with steel core were prepared. This particle was then subjected to periodic magnetic field in upwards direction. As the applied frequency of oscillations is varied, the value of the amplitude of the particle changes. At 10 Hz, the particle shows highest amplitude and thus that corresponds to the resonant frequency of the particle. The density of this particle is lower than the solid steel particle. It can also be seen that as the frequency increases oscillations, decay exponentially which is similar to forced mass spring damper behavior. The amplitude reduces as the increase in velocity increases the drag force on the particle.

4.3.2 2 mm Particle on Corn-Oil Water Interface

It is interesting to note that this phenomenon is valid for variety of interfaces. When 2 mm particle was used on corn oil-water interface it exhibits same behavior as air water interface. The particle was dropped on the water interface prior to adding oil on the water interface. When the frequency was applied the particle oscillated about its equilibrium position along the corn oil-water interface.

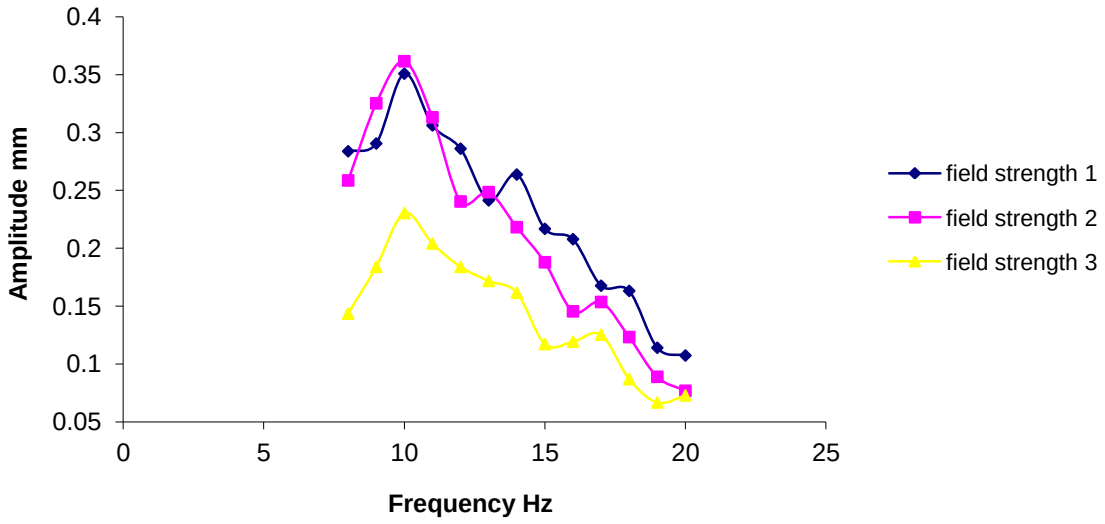

Figure 4.5 Plot of amplitude of oscillation vs. frequency for 2 mm bead on Corn Oil water interface.

The major differences between corn oil-water interface compared to air water interface is that the corn water interface shows higher damping by reduction in amplitude. Corn water interface tension is also significantly lower than air water interface, resulting in higher amplitudes. The particle inertia has a larger impact in this case and it over shoots equilibrium more than it did with the air-water interface, giving higher amplitude at resonance.

4.3.3 Frequency as a Function of Particle Diameter

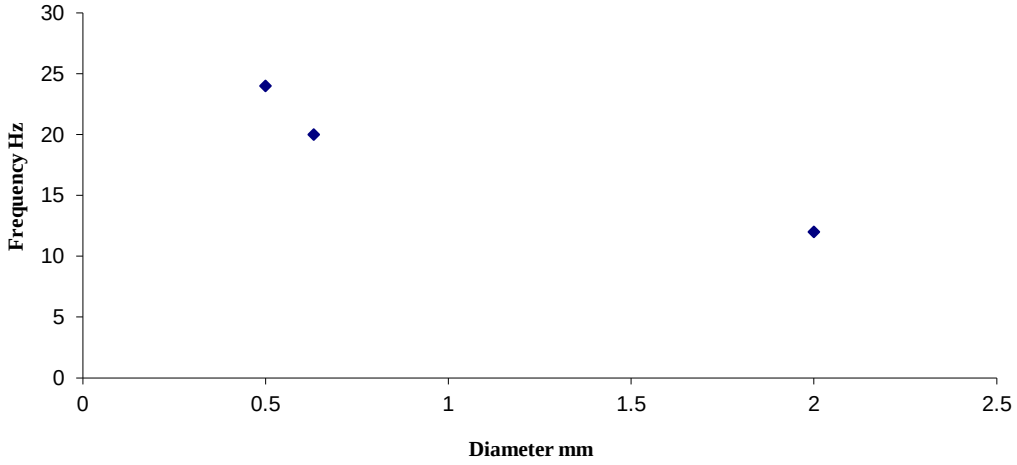

Figure 4.6 Plot of natural frequency vs. diameter of particle on air water interface.

The frequency of oscillation at which amplitude is maximum is plotted as a function of diameter of the particle. It can be seen that the resonant frequency of the particle increases as the size of the particle increases. This is consistent with the past experiments performed by [8] where the particles were dropped on the air-water interface.

CHAPTER 5

DISPERSION OF PARTICLES ON FLUID-LIQUID INTERFACES

This chapter briefly describes some of the key experimental and theoretical results reported in [8] for the motion and dispersion of particles after they come in contact with a liquid surface. It begins with a description of the lateral flow induced due to the adsorption of a small number of particles.

5.1 Fluid Motion Induced at the Interface

Experiments show that when a test particle is trapped at an air-water interface, all of the nearby tracer particles on the interface (placed for flow visualization) move outward away from the test particle. The velocity of tracer particles decreases with increasing distance from the test particle. This implies that the test particle induces a flow away from itself on the interface, the strength of which decreases with increasing distance from the particle (see Figure 5.1). Furthermore, the velocity of tracer particles was maximum shortly after the test particle came in contact with the interface and then it decreased with time. For a tracer initially at a distance of 2.05 mm from the center of the test particle, the velocity decayed to approximately zero at t=0.8 s (see Figure 5.2). The results obtained for a mixture of 60% glycerin in water were qualitatively similar except for that the velocity of tracer particles was smaller. This was expected since the viscosity of the glycerin mixture is larger than that of water and the interfacial tension is smaller.

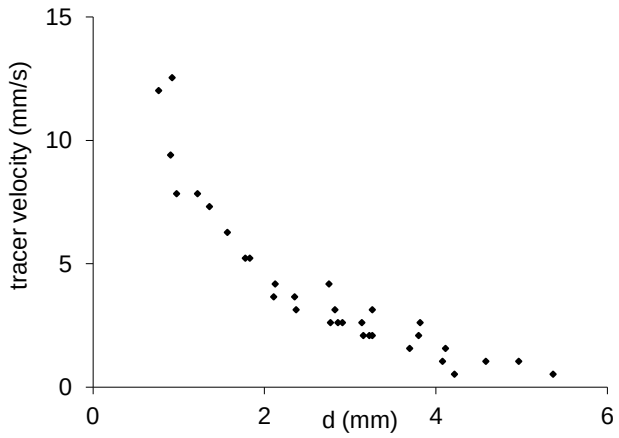

Figure 5.1 The velocity of tracer particles on the air-water interface is plotted as a function of the distance (d) from the center of a glass test particle. The velocity distribution plotted here was recorded at a time 0.033 s after the particle was trapped at the interface. The data were taken for 7 different test particles of the same approximate diameter of 850 μm.

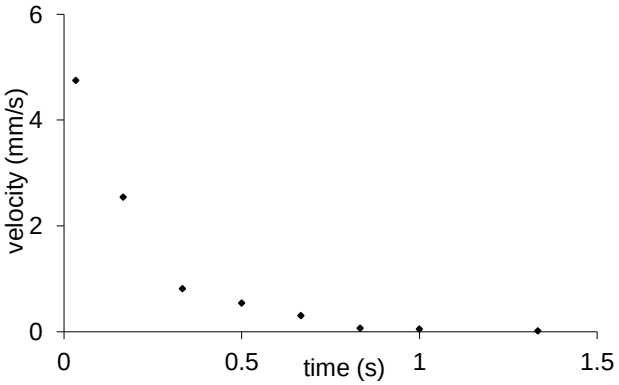

Figure 5.2 The velocity of a tracer particle on the air-water interface initially at a distance of 2.05 mm from a glass test particle of diameter 850 μm is shown as a function of time. The velocity became negligibly small at t = ~0.8 s.

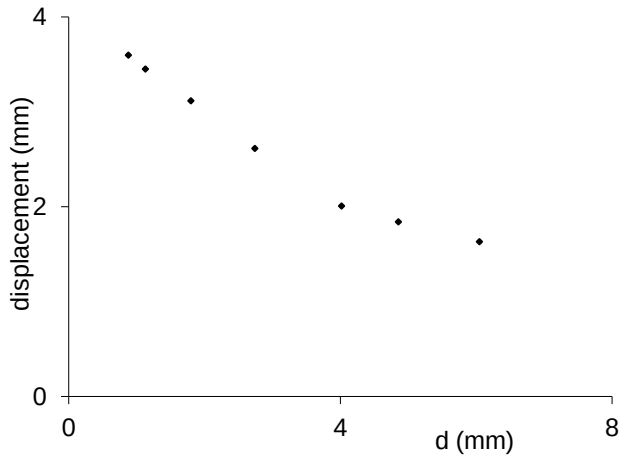

Figure 5.3 The distance traveled by tracer particles on the air-water interface is plotted as a function of their initial distance from the glass test particle. The diameter of the test particle was 850 μm and that of the tracer particle was 100 μm.

The total distance traveled by a tracer particle (away from the test particle) depends on its initial distance from the test particle. Figure 5.3 shows that a tracer particle initially at a distance of 1 mm from a test particle of diameter 850 μm moved a distance of 3.4 mm and that this value decreased as the distance from the test particle increased. This implies that a test particle creates a circular space free of tracer particles the radius of which can be more than four times its own diameter.

The interfacial fluid velocity induced was larger when two identical glass test particles were simultaneously dropped onto the air-water interface (see Figure 5.4). The motion of tracer particles in this case was approximately radially outward from the middle of the line joining the centers of the test particles. The net flow induced at the interface (measured using tracer particles) is stronger when two particles were dropped as each particle creates its own radially outward flow resulting in a net flow which can be approximated as the sum of the flows caused individually by the dropped particles.

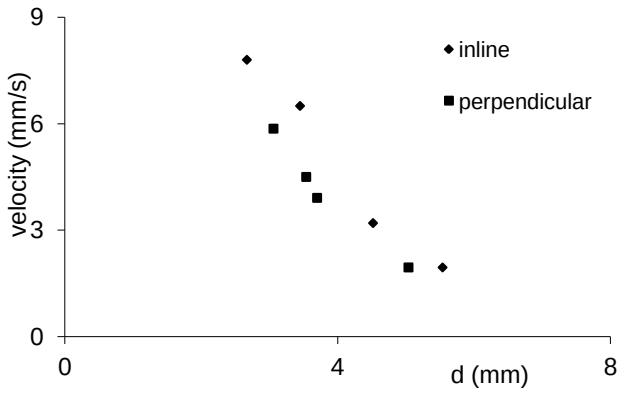

Figure 5.4 The velocity of tracer particles on the air-water interface is plotted as a function of the distance (d) from the mid-point of the line joining the centers of the two test particles. The diameter of the particles was 850 μm and the initial distance between them was 0.91 mm. The velocities shown here were recorded at a time of 0.033 s after the particles were trapped at the interface. The velocities of the tracer particles are shown along the directions inline (parallel) and perpendicular to the line joining the centers of the particles

Furthermore, the velocity of tracer particles in Figure 5.4 was larger than in Figure 5.1 where only one particle was dropped. This implies that the net flow induced at the interface (measured using tracer particles) is stronger when two particles were dropped. This is due to the fact that each particle creates its own radially outward flow, resulting in a net flow which can be approximated as the sum of the flows caused individually by the dropped particles. The other features of the induced flow were qualitatively similar to that for one particle.

5.2 Lateral Motion of Particles

When two test particles were dropped together, they moved away from each other along the line joining their centers. Figure 5.3 shows that the separation velocity decreased with increasing time, and the velocities of the two particles were approximately equal in magnitude. The relative velocity with which particles separated decreased with increasing

initial distance between them. Furthermore, after some time, larger sized particles reversed their direction to come back to cluster under the action of attractive lateral capillary forces that arise because of the particles' buoyant weight. The velocity with which they came back, however, was significantly smaller than the velocity with which they dispersed. Micron sized particles for which lateral capillary forces are negligible, however, remained dispersed.

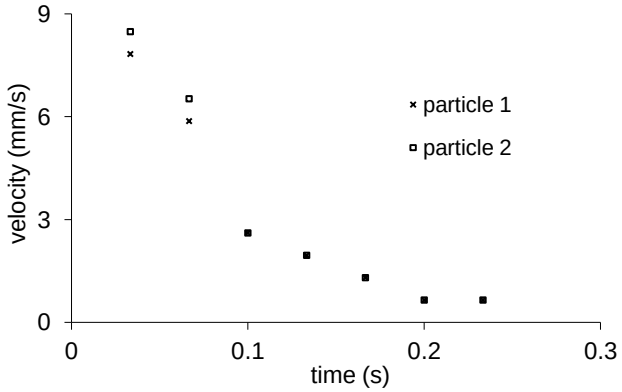

Figure 5.5 The velocity of two glass particles of diameter 850 μm dropped simultaneously onto the air-water interface is shown as a function of time. The initial distance between the particles was 1.21 mm. After becoming trapped in the interface, they moved apart approximately along the line joining their centers. The magnitude of the velocities of the two particles was approximately equal.

The velocity with which two glass particles of the same size moved apart was larger than the velocity with which a tracer particle placed at the same distance moved away when a single glass particle was dropped. This is noteworthy because the larger glass particles have a larger mass and are thus expected to move slower and not faster. However, they moved apart faster because of the repulsive hydrodynamic forces that arise because of the particles motion in the direction normal to the interface which causes the fluid to squeeze through the gap in between them.

In both experiments and direct numerical simulations, when a test particle was dropped near an identical particle which was already trapped within the interface, the trapped particle moved away along the line joining their centers, but the test particle did not move significantly. This indicates that the test particle creates a flow on the interface away from itself causing the particle already trapped to move away.

Now consider the case when four particles were dropped onto a liquid surface. The goal is to determine the dependence of the dispersion velocity of particles on the number of particles. In Figure 5.6, the velocities of four glass particles dropped together onto an air-water interface are plotted as a function of time. The diameter of these test particles was 650 μm. The particles moved apart approximately along radial lines emanating from the center of the cluster. The velocities were different because the initial distances between the test particles were not the same and could not be controlled in the experiments. The average velocity with which the particles moved apart was larger for four than for two particles. This shows that the velocity with which particles dropped onto a liquid surface move apart depends on the number of particles dropped.

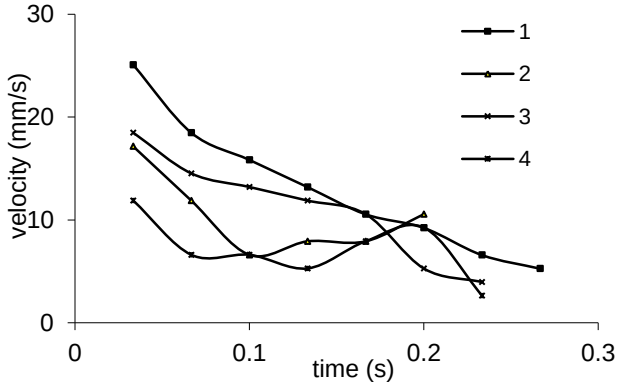

Figure 5.6 The velocities of four glass particles simultaneously dropped onto an air-water interface. The particles moved apart approximately along radial lines emanating from the center of the four particles. The diameter of particles was 650 μm. The initial average distance between the four particles was around 1.0 mm.

The experiments also show that when more than two particles are dropped together they move apart (or disperse) approximately along radial lines emanating from the center of the cluster. The average velocity with which particles dispersed increased as the number of particles sprinkled onto the liquid surface increased in both experiments (see Figure 5.7) and direct numerical simulations (see Figure 5.8). In the latter, the maximum of the velocity with which particles dispersed was reached shortly after they came in contact with the liquid surface. After that point, the velocity slowly decreased with time. Furthermore, when a cluster of particles was sprinkled onto a liquid surface, all of the particles moved outward from the cluster center (see Figure 1.1 which shows the streak lines of the particle motion) and the velocity with which the cluster expanded increased with increasing cluster size.

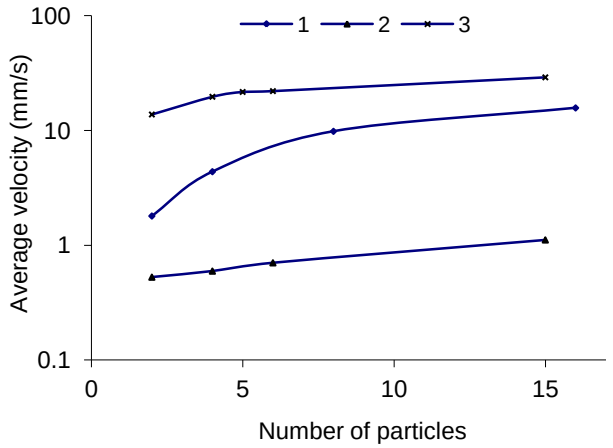

Figure 5.7 The average velocity with which glass particles moved apart 0.033 s after coming in contact with an interface as a function of the number of particles. The case marked "1" is for 850 μm glass particles sprinkled on water, "2" is for 650 μm glass particles sprinkled on 60% glycerin in water, and "3" is for 650 μm glass particles sprinkled on corn oil.

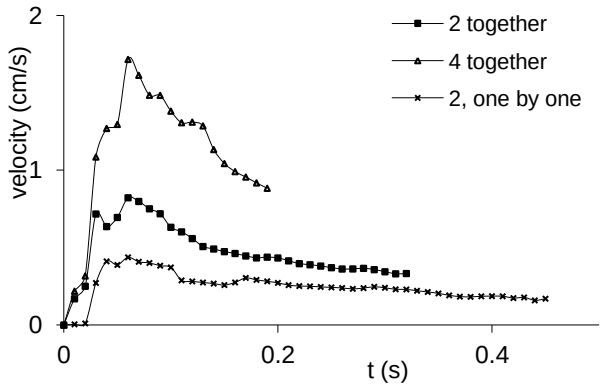

Figure 5.8 The lateral velocity of the particles is shown as a function of time. The cases shown are: (i) Two particles released together at a height of 0.95*R* above the undeformed interface. The initial distance between the particles was 3.2*R*. (ii) Four particles released together at a height of 0.95*R* above the undeformed interface. The initial positions of the four particles formed the vertices of a square with sides 3.2*R*. (iii) One particle released at a height of 0.95*R* above the undeformed interface, and the center of the second one was at the undeformed interface. The horizontal distance between the particles was 3.2*R*. The velocity of the latter particle is shown while the velocity of the particle released above the undeformed interface was negligible.

CHAPTER 6

FLOW VISUALIZATION AND MEASUREMENT

6.1 Introduction

The transient flow that arises when a particle is adsorbed on a fluid-liquid interface flow can be divided into two broad regions: the interface region and the region below the interface. Two different flow visualization experiments have been conducted to understand the nature of flow in these regions. The flow on the interface is particularly interesting as studying it helps in understanding various natural phenomena like ruppia pollen spreading on a water surface [8, 15]. This flow can be easily visualized by seeding the interface with tracer particles and observing their motion when a test particle is adsorbed in the interface. The velocity of these tracer particles can be assumed to the same as the fluid velocity at the interface as they are small in size and therefore follow streamlines. These results are discussed in Chapter 5.

The flow below the interface is more difficult to measure and requires a non-intrusive technique. In this study it is measured using the PIV technique which is described in this chapter. Clearly, the complete three-dimensional nature of the flow is essential to fully understand the mechanism by which a newly adsorbed particle creates flow away from itself on the interface.

There are several methods available that can be used for measuring the fluid velocity, for example, Laser Doppler Velocimetry (LDV), hot wire, and Particle Image Velocimetry (PIV). The first two of these methods are not well suited for this study as they only allow for the point-wise measurements. In our experiments we are required to

measure the transient velocity distribution in a plane in which the particle is adsorbed. Only the Particle Image Velocimetry (PIV) technique allows for such measurements. Since PIV gives the velocity distribution on a plane, it also gives a visual representation of the induced flow. Flow visualization is an important tool in experimental fluid mechanics. It not only enhances our qualitative understanding of complex flows, but also helps us in understanding their dynamical behaviors.

As noted, PIV is an optical flow measurement technique that allows one to measure the velocity field over a planer surface. This chapter describes the transient flow that arises in a vertical plane due the adsorption of a spherical particle and its strength is measured as a function of time.

6.2 Brief History of PIV

PIV originated from primitive flow visualization techniques. For example, over the centuries the speed of water in a river has been estimated by observing floating objects. It is a simple approach, but can be used to obtain a good estimate of the flow rate in a river, as well as the flow patterns. One can visualize eddys and the formation of vortices as water goes around rocks. Ludwig Prandt used particles to study fluid motion in the first decade of the 20^{th} Century [47]. He performed experiments in 1904 to study the flow in a water tunnel. The water surface was seeded with mica particles. He visually observed the flow, but did not obtain any quantitative data. The motion of seeded particles was used to get an estimate of the fluid velocity and to understand and demonstrate phenomena like laminar and turbulence flows, separation, boundary-layer effect, streamlines, etc. The

PIV approach uses this concept of seeding the fluid with particles that can be tracked to calculate the fluid velocity.

In the last two decades tremendous growth has taken place in computational and optical sciences making analysis of large data sets possible. For example, it is possible to take pictures at rates up to 1 million frames per second. It is also possible to take multiple high resolution images and compare them with each other to obtain the velocity distribution using advanced computational techniques. This growth in computational and optical fields has led to advances in measurement techniques. Currently, PIV is widely used in fluid mechanics to measure and visualize flow fields of both gases and liquids. For example, in aerodynamics it is used to understand unsteady flows. The technique is also used in the design of propellers and aerofoils.

In the beginning, the PIV technique was used to study only two-dimensional (2D) flow fields. By the 1990s, with the aid of multiple cameras and lasers, the technique was extended for three-dimensional (3D) flow fields. Currently, there are commercially-available PIV systems that can measure the velocity field within a fluid volume. This technique is called the volumetric PIV technique. It has opened new doors in the field of experimental fluid mechanics allowing investigation of flows that could not be studied using earlier techniques.

The next section describes a 2D PIV system that is used to measure the flow induced by the adsorption of a particle. This will be followed by a description of the computational approach used to analyze the PIV data.

6.3 Experimental Setup and Components of PIV System

This section describes the experimental setup and the main components of a 2D PIV system. The approach involved seeding fluid with tracer particles, and then dropping a test particle onto the fluid surface and measuring the fluid flow which was induced. A brief description of the measurement technique and the method used to select the interrogation area is also discussed in this section.

6.3.1 Experimental Setup

The setup consists of a square Petri dish which was partially filled with water. Figure 6.1 shows the top view of the setup. The laser sheet is normal to the camera axis and is the plane on which flow measurements are performed. The test particle is dropped in this plane. The particle remained in this plane while oscillating vertically and inducing a flow. The camera was mounted such that it was in-line with the water surface. This position of the camera gives an undistorted view of the volume directly below the water surface.

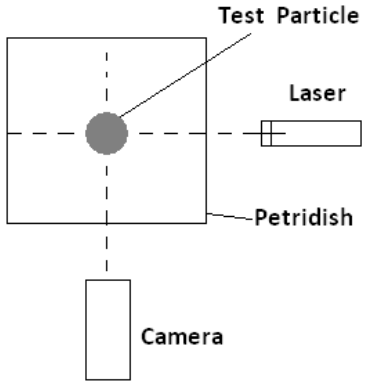

Figure 6.1 Schematic diagram of the experimental setup. The laser sheet is perpendicular to the interface and the camera axis. The test particle is dropped near the intersection of the axis of the camera and the laser sheet.

The fluid in the Petri dish was seeded with small tracer particles. Silver coated hollow glass spheres of density around 1gm/cc were used. The density of seeding particles was matched closely to that of the fluid to ensure that they did not sediment to the bottom of the device. The average size of tracer particles was around 20 μm. Thus, it is reasonable to assume that these particles follow the flow because their size is small and also because their density is approximately equal to the density of the fluid. Seeding particles were coated with silver to scatter the laser light. This is important because the size of a tracer particle is small and so if it is not silver coated the scattered intensity would be too small to see the particle.

The test particle is dropped on the interface at a point where the laser sheet and the camera axis intersect. The flow that is induced causes seeded particles to move. A high speed camera is used to capture the motion of these seeded particles. The velocity of the seeded particles is than calculated using the procedure described in Sections 6.3.5 – 6.3.10.

6.3.2 Camera

The motion of tracer particles is recorded using a Casio EX F1 high-speed camera. This camera is capable of recording at various speeds and resolutions. The available options are: 1200 frames per second (fps) at the resolution of 336 x 96 pixels, 600 fps at the resolution of 432 x 192 pixels, 300 fps at the resolution of 512 x 384 pixels and 60 fps at the resolution of 1920 x 1080 pixels. The fluid velocity, the size of the field of view, the zoom, the seeding density and the size of interrogation area determine the frame rate that is needed to optimally measure the induced flow. For measuring the flow at the interface

the frame rate of 300 was needed, as the fluid velocity on the surface is relatively larger. A short distance away from the interface the frame rate of 60 fps was found to give good results.

The camera lens is capable of providing a zoom of 432 mm. Multiple close-up lenses were used to decrease the focal length of the camera so as to magnify the image. All the experiments performed had a field of view of approximately 10 mm x 10 mm, or less. Since a high zoom setting and multiple close-up lenses were used, the images contained optical aberration near the edges and thus the data close to the edges had reduced accuracy.

6.3.3 Laser

A 40mW solid-state diode laser was selected to illuminate the vertical plane. The intensity of the laser could be varied by using a secondary power supply. The wavelength of the laser was 532 nm which is visible as green light. The optics in front of the laser contains a spherical and a cylindrical lens to produce a thin laser sheet as shown in Figure 6.2. The laser beam originates from the diode as a line which is compressed by the spherical lens to form a thin laser beam. This thin beam is then expanded into a thin laser sheet by the cylindrical lens. The thickness of the sheet is around a few microns. It is important to note that a stronger laser would have been required if a larger field of view was used for flow measurements.

.

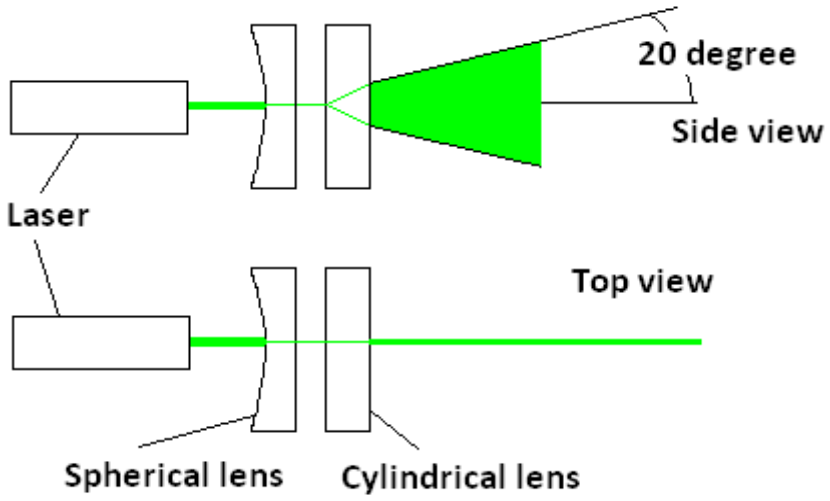

Figure 6.2 Schematic of the setup used to illuminate a plane with laser light. A combination of the spherical and cylindrical lenses produces a thin laser sheet as seen in the top view. The laser sheet expands at an angle of 20 degrees as it comes out of the cylindrical lens.

6.3.4 Seeding Particles

The liquid used in this study was water. It was seeded with tracer particles. The density of seeding particles was matched closely with the water density. The seeding particles were silver-coated hollow glass spheres of density around 1.07 gm/cc, and their average size was around 20 μm. They were mixed in DI water to make a solution. Only those particles that remained suspended for 3 hours were used in the experiments. Since the densities of

water and the seeding particles were very close and the size of particles is small, it is reasonable to assume that they followed the fluid by moving along the streamlines.

Since seeding particles are silver-coated, they were clearly visible as they intensely scatter the laser beam. Therefore, their trajectories could be followed, which is required for the PIV approach. The scattering intensity of a particle is proportional to its surface area. The scattering intensity also depends on the wavelength of light. The laser intensity was held fixed for the experiments.

6.3.5 Measurement Technique

Several computational methods are available to obtain the velocity distribution from a sequence of PIV images. The autocorrelation and cross-correlation based methods are the two most-commonly used methods. The autocorrelation-based method is used to analyze a sequence of double-exposed images which contain particles positions at two different times. The main disadvantage of the autocorrelation method is the uncertainty of the flow direction. This uncertainty causes errors which make the velocity distribution noisy. The cross-correlation based method uses two images taken at two different times for obtaining the velocity. It compares the images to evaluate the direction and magnitude of the particle velocities. To perform these correlations, the image is divided into interrogation areas. This latter approach is used in our PIV analysis.

Furthermore, for our experiments, the velocity varied with time and so time-resolved measurements were required. This involved recording the motion of tracer particles at sufficiently-high frame speeds, and then obtaining the velocity distribution from the motion of tracer particles within two consecutive frames.

6.3.6 Interrogation Area and Velocity Distribution

To compute the fluid velocity distribution within the area of a frame, the frame is divided into rectangular areas of fixed pixel length and width. These rectangular areas are referred to as the interrogation areas. In the cross-correlation technique which is used in our analysis, the pixels of an interrogation area are compared with the corresponding pixels of the next frame. The peak of the cross-correlation defines the average distance travelled by the tracer particles during the elapsed time between the frames. Since the time difference between the frames is known, the average velocity of tracer particles is obtained by dividing the distance travelled by the time between the frames. This average velocity is assumed to be the fluid velocity at the center of the interrogation area.

The approach works best when there are 7 to 8 seeded particles in the interrogation areas. As the size of the interrogation area decreases, the accuracy increases but the processing time for the frame increases. Also, below a critical value, a decrease in the interrogation area produces excessive noise. Therefore, depending on the parameters like the resolution of the sensor, optics, and laser intensity, there is a critical size of interrogation area for which the signal to noise ratio is optimal.

The distribution of the fluid velocity for a frame is obtained by adding the velocities for all of the interrogation areas of that frame. An example of a velocity field obtained using this approach is shown in Figure 6.4.

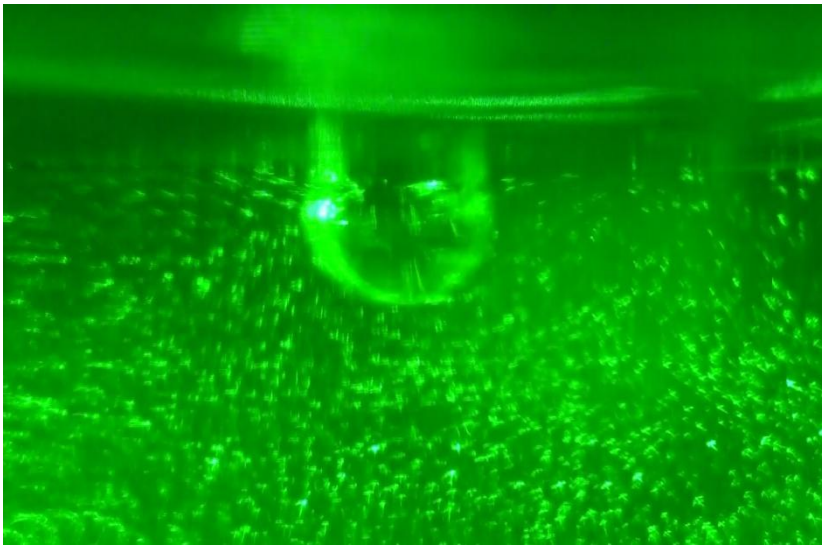

Figure 6.3 Velocity distribution 0.3 s after a test particle touches the interface. The figure shows the seeded particles and the air water interface.

6.3.7 Cross-Correlations and the FFT Approach

The average displacement of particles within an interrogation area is obtained using a two-step method. First, the Fast Fourier Transform (FFT) approach is used to obtain the cross-correlations for the interrogation areas. The location of the peak in the FFT is used to obtain the peak of the cross-correlation. However, since the data is discretized, the peaks are not necessarily at the discretized values for which the data is available. The data was therefore interpolated to obtain a better approximation of the peak value. The size of interrogation areas used for the results presented in thesis is 96 x 96 pixels.

6.3.8 Image Intensity Field

The image intensity field at *x* due the presence of *N* particles can be written as

$$I(x) = \sum_{i=1}^{N} V_o(X_i)\, \tau(x - x_i) \tag{6.1}$$

where $V_o(X_i)$ is the light energy of an individual particle *i* and $\tau(x)$ is the point spread function of the imaging lens which is assumed to be a Gaussian function. The particles are assumed to be point particles since they are small and not resolved in PIV images.

6.3.9 Cross-Correlation of Two Images

Assume that in the second image taken after a time interval of ΔT all of the particles in the interrogation area have moved by a constant distance of D. Thus, the image intensity field for the second image is given by

$$I'(x) = \sum_{i=1}^{N} V_o\,(X_i + D)\, \tau(x - x_i - d) \tag{6.2}$$

Here d is the distance moved in the image coordinate system and $V_o\,(X)$ is the light energy function for the second image which is assumed to be the same as for the first image.

The cross-correlation function of the two interrogation areas can be written as

$$R(s,D) = \frac{1}{a_I} \sum_{i,j} V_o(X_i) V_o(X_i + D) \int_{a_I} \tau(x - x_i)\, \tau(x - x_j + s - d)\, dx \tag{6.3}$$

Where a_I is the interrogation area and ***s*** is the separation vector in the correlation plane. The above cross-correlation contains can be decomposed into three parts. The first part is the convolution of the mean intensities and the second the fluctuating noise part. The following part gives the component of the cross-correlation function that corresponds to the correlation images of the same particles from the two images

$$R_D(s,D) = R_\tau(s-d) \sum_{i=1}^{N} V_o(X_i) V_o(X_i + D) \tag{6.4}$$

Here $R_\tau(s)$ is the auto-correlation function of a particle image with itself which is a Gaussian function. Therefore, the cross-correlation peak is at ***s*** = ***d***. The location of the peak thus gives the average displacement of particles within the interrogation area.

The average displacement d and the time elapsed (ΔT) between the frames gives the average fluid velocity for the interrogation area

$$\mathrm{u} = \frac{d_x}{\Delta T} \tag{6.5}$$

$$\mathrm{v} = \frac{d_y}{\Delta T} \tag{6.6}$$

Here u and v represent the velocity components in x and y directions, and d_x and d_y are the components of ***d***. This analysis is performed on each of the interrogation areas to obtain the velocity distribution for the image, and repeated for the entire sequence of frames to obtain the time dependent behavior of the fluid velocity. The auto-correlations are obtained using the FFT (Fast Fourier Transform) approach.

6.3.10 PIVLAB

There are several open-source codes available for performing the PIV analysis described above on a sequence of frames. PIVlab was used for time resolved measurements presented in this dissertation. It uses the MatLab toolboxes for image processing and for performing fast Fourier transforms. The PIVlab code was adapted to meet the needs of our experiments.

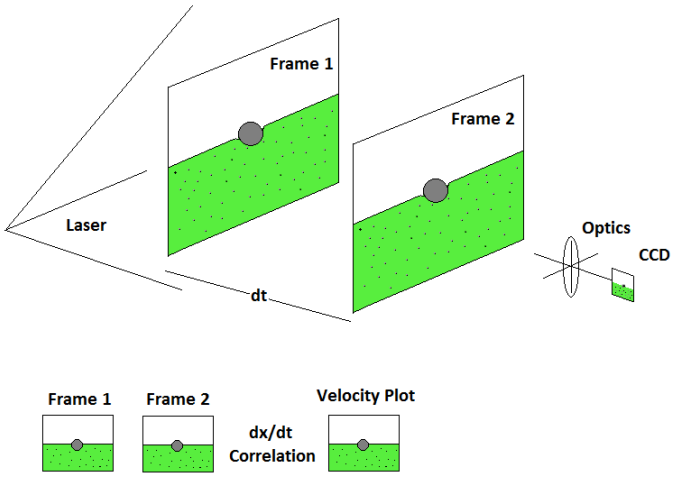

Figure 6.4 Schematics of the experimental setup. The laser illuminates fluid on a thin plane. The camera records frames at the required frame rate. The PIVlab algorithm selects the interrogation area in the frame and determines the velocity distribution within the frame.

6.4 Experimental Results

As noted earlier, when a test particle comes in contact with a water surface the vertical capillary force pulls it into the interface causing it to accelerate to a relatively-large velocity normal to the interface. Since the motion of the particle on the surface of mobile liquids like water is inertia dominated, it oscillates vertically several times about its equilibrium height before the viscous drag causes its motion to stop. The test particle itself however does not move laterally. This vertical motion of the test particle gives rise to a lateral flow on the interface away from the particle. This flow has been measured for particles ranging in size from a few micrometers to a few millimeters [8]. The aim of this

chapter is to describe the complete three dimensional nature of the flow induced by the adsorption of a spherical particle on an air-water interface.

The measurements show that a millimeter sized particle oscillates for about 0.1 s after coming in contact with a water surface. The flow these oscillations induce however persists for several seconds. The induced flow is strongest near the interface, and is accompanied by waves on the interface that travels at speeds of around 300 mm/s. The flow below the interface builds up relatively slowly which perhaps is a consequence of the fluid's inertia. The primary focus of this chapter is on the visualization and measurement of the transient flow starting just below the interface. The flow on the interface was difficult to analyze using a camera mounted on a side due to the curvature of the interface.

6.4.1 Velocity Distribution

Figure 6.5 shows the velocity distribution in the plane of the laser sheet 0.383 s after a 2 mm glass particle came in contact with an air-water interface. The particle touched the interface and oscillated vertically to generate the flow. The figure shows that the flow near the interface is away from the particle. This is in agreement with the surface velocity measurements performed using small tracer particles discussed in earlier chapters. The figure also shows that the fluid directly below the particle rises up towards the particle. Near the interface the flow turns sharply away from the particle and becomes directed tangential to the interface as seen in Figures 6.6 and 6.7. The velocity near the interface is an order of magnitude larger than a diameter away from the particle. The

velocity distribution is approximately axisymmetric about the vertical line passing through the center of the particle.

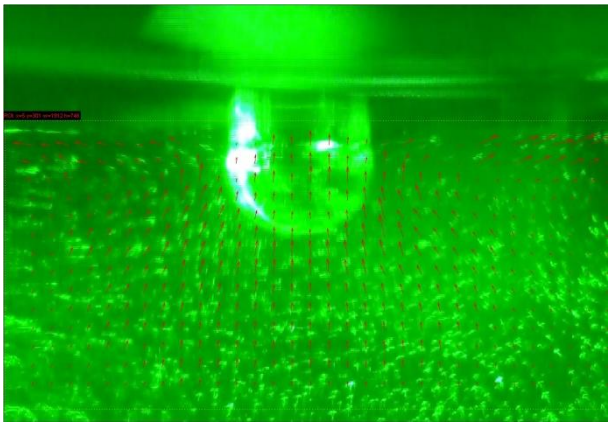

Figure 6.5 Velocity field 0.383 s after a 2 mm glass particle came in contact with the air-water interface. The particle was dropped such that its center was approximately in the middle of the laser plane. The velocity distribution is approximately axisymmetric about the vertical passing through the center of the particle.

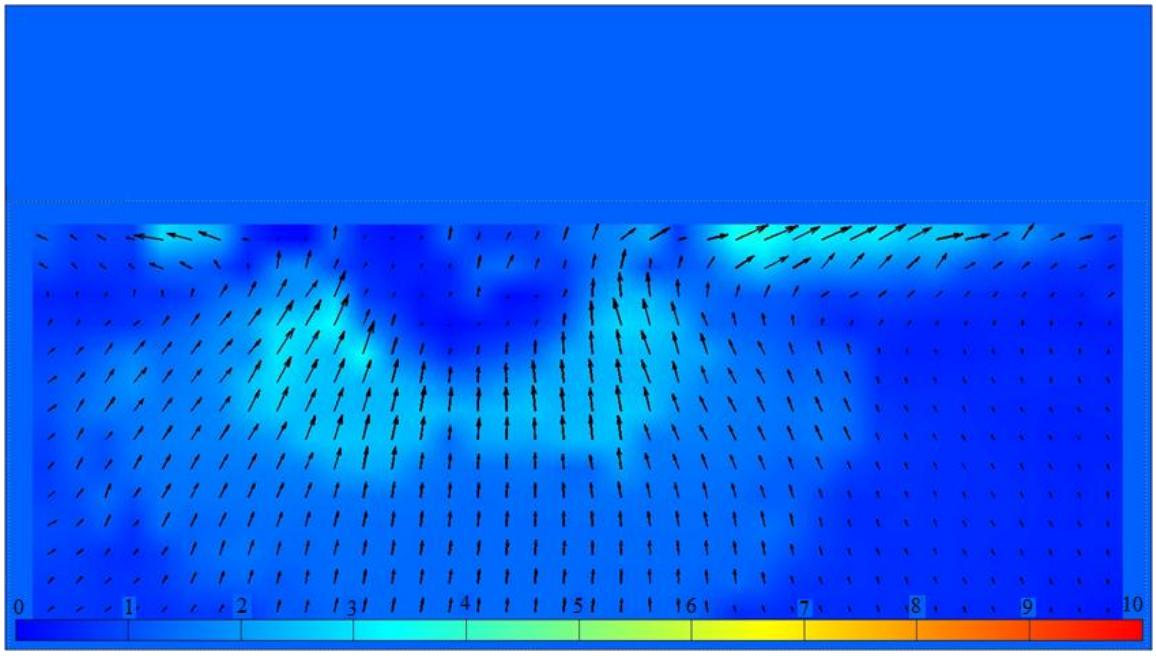

Figure 6.6 Velocity field and its isovalues 0.38 s after a 2 mm glass particle came in contact with the air-water interface.

The velocity in the region occupied by the particle is small but not zero. The measured velocity is non-zero, even though the test particle is not moving, because tracer particles in front of and behind the test particle are visible and moving. The PIV technique detected these moving particles to give a non-zero value of the velocity. The size of the interrogation area is another important parameter. As noted earlier, the velocity vectors represent the average velocity for the interrogation areas and are shown at their centers. The size of the interrogation area in Figure 6.5 was small compared to the projected area of the test particle. Specifically, the interrogation area had a size of 96 x 96 pixels and those dimensions were approximately 1/5 times the diameter of the test particle. Therefore, for some of the interrogation areas near the boundary of the particle

the velocity was computed over an area that was not entirely contained within the particle.

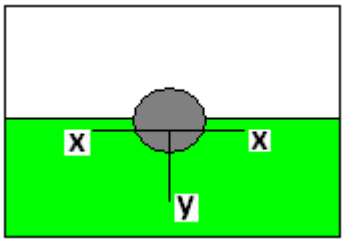

Figure 6.7 Represents the x and y axis along which the data is plotted.

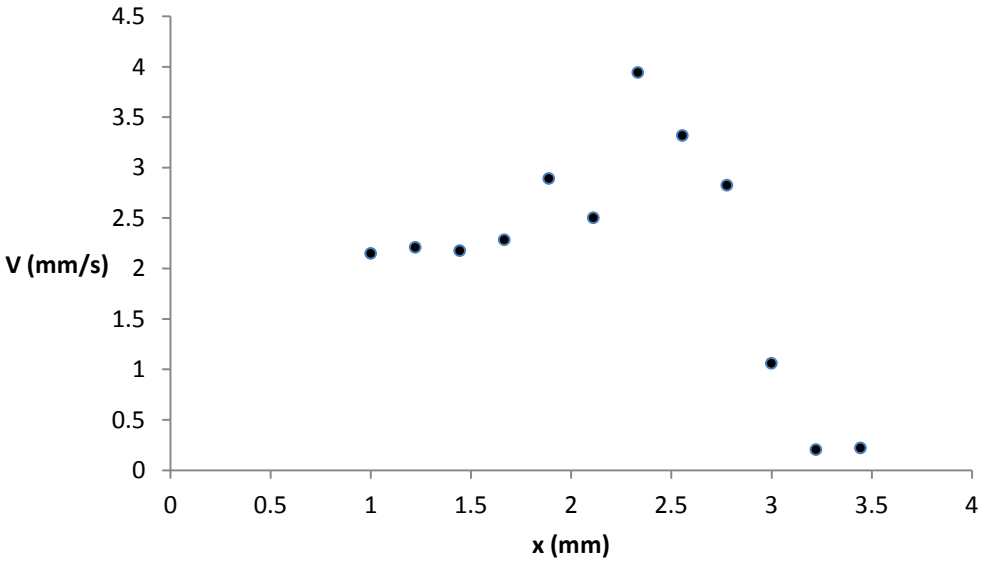

a) Horizontal component of velocity at a distance of 0.1 mm from the interface as a function of distance from center of particle. The distribution on the left side of the particle is shown.

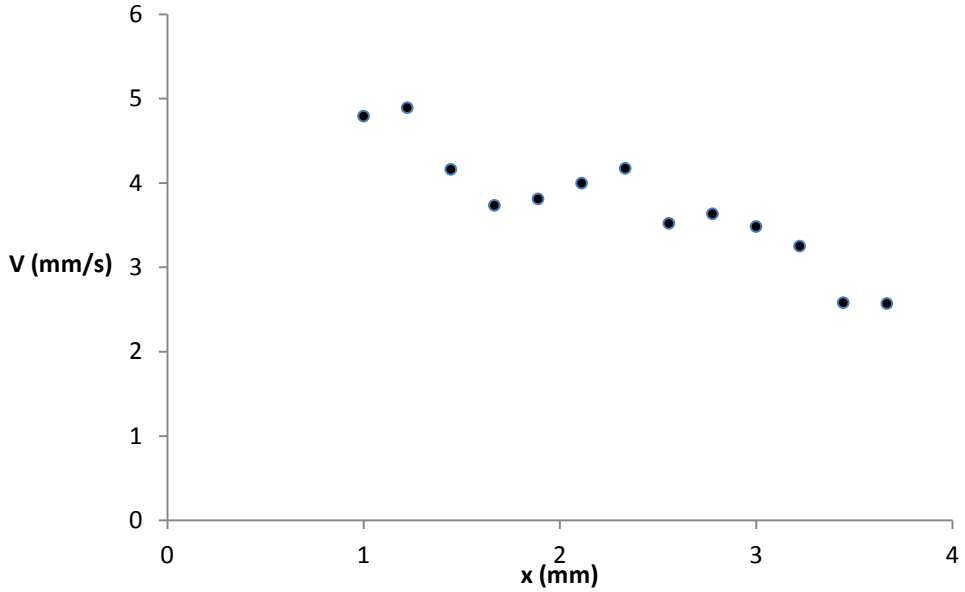

b) Horizontal component of velocity at a distance of 0.1 mm from the interface as a function of distance from center of particle.. The distribution on the right side of the particle is shown.

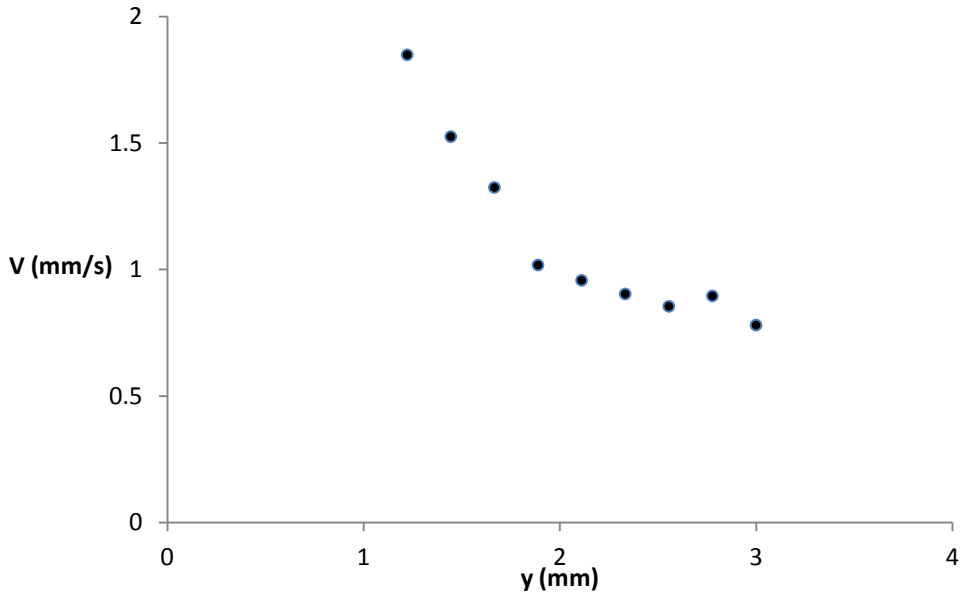

c) The verticle component of velocity is shown as a function of verticle distance from center of particle. The distribution on the left side of the particle is shown.

Figure 6.8 Fluid velocity plotted as a function of distance from the center of the particle. The figure shows velocity 0.5 s after the particle came in contact with the interface.

6.4.2 Transient Velocity Distribution

Figure 6.8 describes the transient development of the flow due to the adsorption of a 2 mm glass particle on an air-water interface. The recording speed was 60 fps, and the consecutive frames were used to obtain the velocity distribution. The time was measured from the moment the test particle came in contact with the interface. The velocity vectors are shown on a vertical plane passing approximately though the center of the particle. The width of the laser sheet is comparable to the diameter of the test particle. The figure shows that flow is symmetric about the vertical line passing through the center of the particle.

The first two photographs in the sequence taken at t = 0.167 and 0.25 s show that the flow pattern around the particle is beginning to develop, but the velocity on the interface is already relatively large. The vertical oscillations of the test particle were already damped out at this time and particle had assumed its equilibrium position in the interface. The fluid at a distance of a particle diameter on its sides comes towards the particle center at an angle of about 45 degrees, but in the region below the particle the velocity was small. The direction of flow changes near the particle close to the air-water interface. Since water is an incompressible fluid, continuity implies that the flow rate towards the particle must be equal to the flow rate near the interface away from the particle.

Figures 6.8 c-d at t = 0.38 and 0.78 s show that the distribution of velocity changes qualitatively in that the velocity in the region occupied by the particle is relatively large and the velocity in the region below the particle is also large. The former,

as noted earlier, is a consequence of the fact that tracer particles in front and behind the test particles move upwards and their motion is visible in the PIV images. These measurements indicate that although the test particle itself is not moving, the fluid velocity near the particle surface is relatively large. The fluid rises vertically towards the particle and close to the interface it moves away from the particle. The velocity in the region below the particle is larger than on its sides. The velocity in the latter region was larger in Figures 6.8a-b. In fact, the velocity field at this point in time appears to be similar to that for a biaxial extensional flow.

The flow pattern described above continues to persist in Figures 6.8 e-j, except that the fluid velocity near the particle surface is much smaller. This happens because the test particle is not moving and so according to the no-slip condition the fluid velocity near its surface should be small. This is not the case in Figures 6.8 a-d because just after a particle is adsorbed it induces a flow towards itself. In Figures 6.8 e-j the mechanism that drives the fluid towards a newly-adsorbed test particle is no longer present, and so the fluid velocity near the test particle decreases with time. In fact, the flow strength slowly decreases with time everywhere. The flow pattern of these latter photographs persisted for about 1.00 s but its strength continued to decrease with time.

Figure 6.9 A time sequence of frames showing the fluid velocity distribution as a function of time. The parameters are the same as in Figure 6.5. The velocity vectors are shown on a vertical plane passing though the center of the particle. The flow is axisymmetric about the vertical line passing through the particle center. The velocity magnitude is shown by the lengths of the arrows. The video was recorded at a frame rate of 60 fps. The time shown in the figure is the time elapsed after the particle comes in contact with the interface. The sequence of frames a-k are shown next.

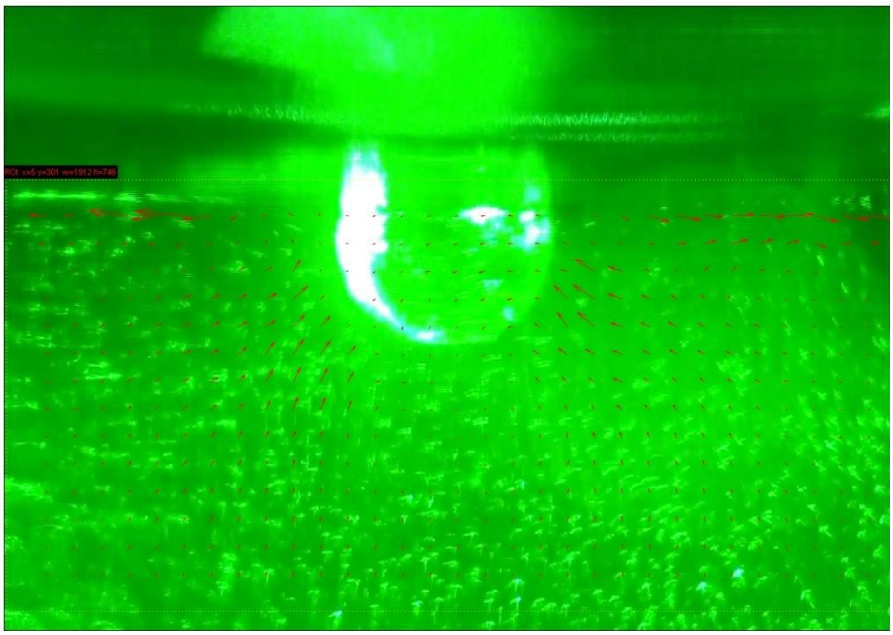

a) t = 0.167 s. Notice that the water velocity below the test particle is small, and the velocity near the interface is relatively larger. The average velocity of the field is 0.499 mm/s.

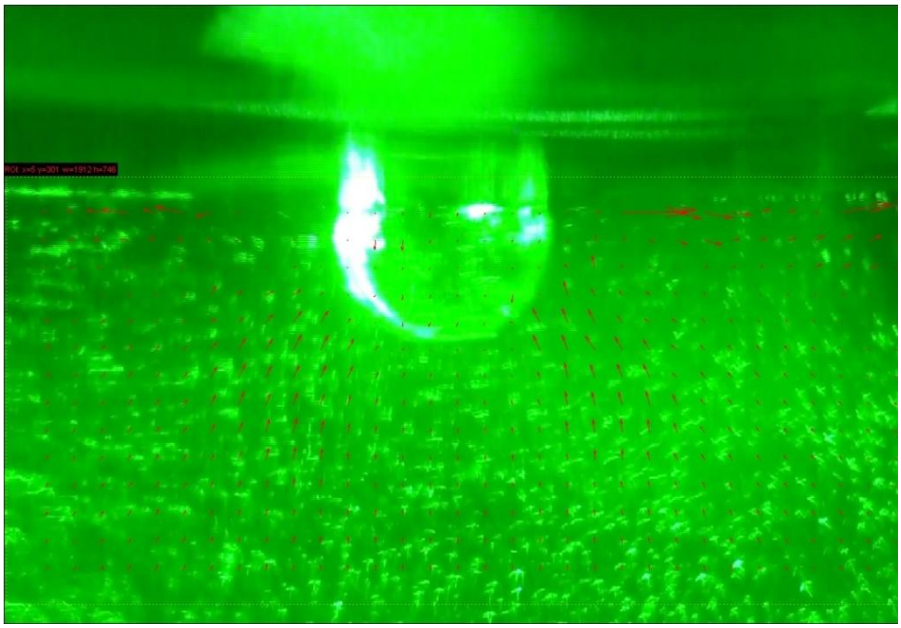

b) t = 0.25 s. The fluid velocity below and around the test particle begins to increase. The average velocity of the field is 0.5826 mm/s.

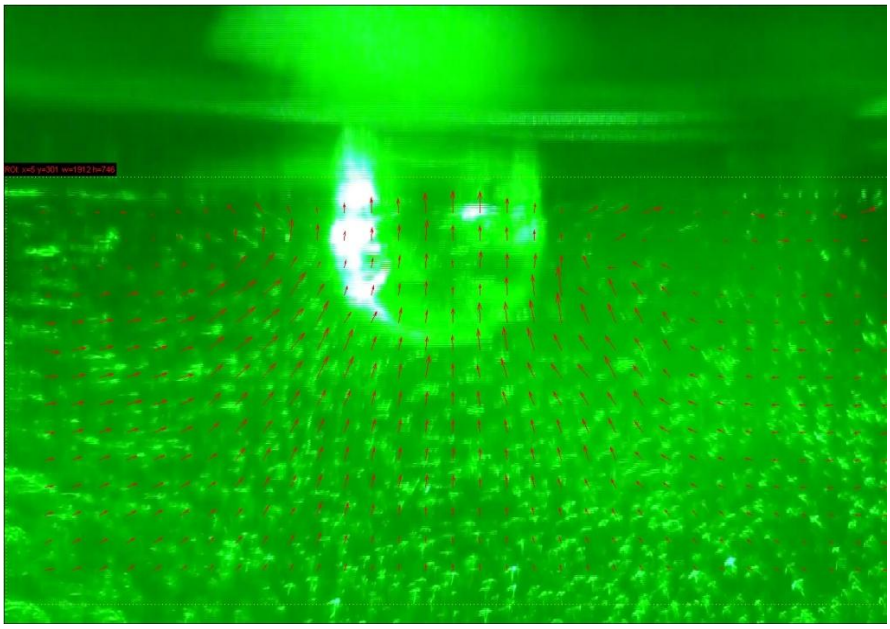

c) t = 0.33 s. The water velocity around the particle and near the interface is relatively large. Notice that the test particle is not moving vertically, but the fluid in its front and back is moving upwards. The 2D PIV technique averages over the depth and so the velocity is a projected average for the region occupied by the particle and the region in front and behind the particle. The average velocity of the field is 0.95 mm/s.

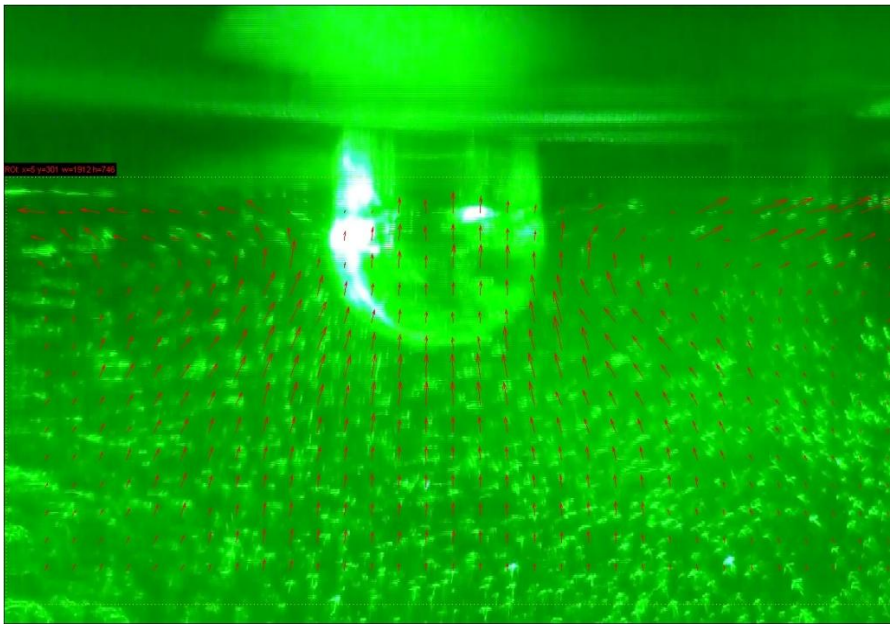

d) t = 0.38 s. The velocity distribution is qualitatively similar to that in the previous photograph. The average velocity of the field is 1.21 mm/s.

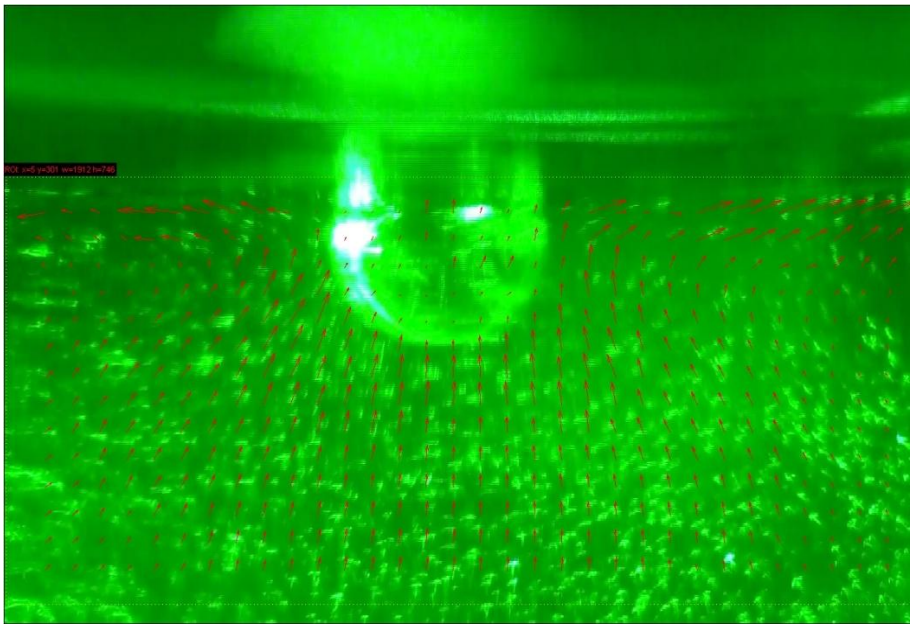

e) t = 0.45 s. The flow pattern is qualitatively similar to the previous two photographs, except that the fluid velocity near the particle is significantly diminished. The average velocity of the field is 1.301 mm/s.

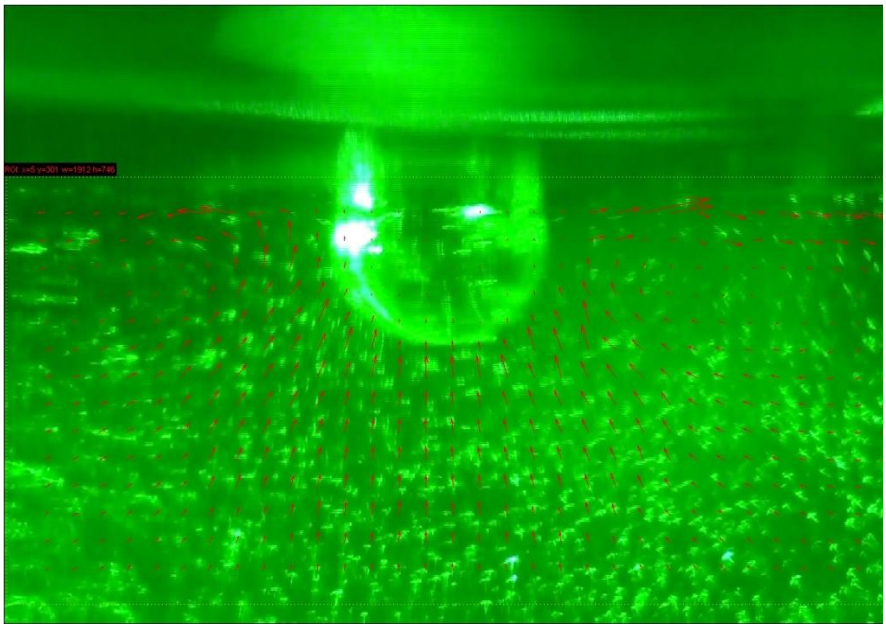

f) t = 0.5 s. The flow pattern is qualitatively similar to the previous photograph. Note that the fluid is rising from below the particle and near the interface it moves away from the particle. The average velocity of the field is 0.956 mm/s.

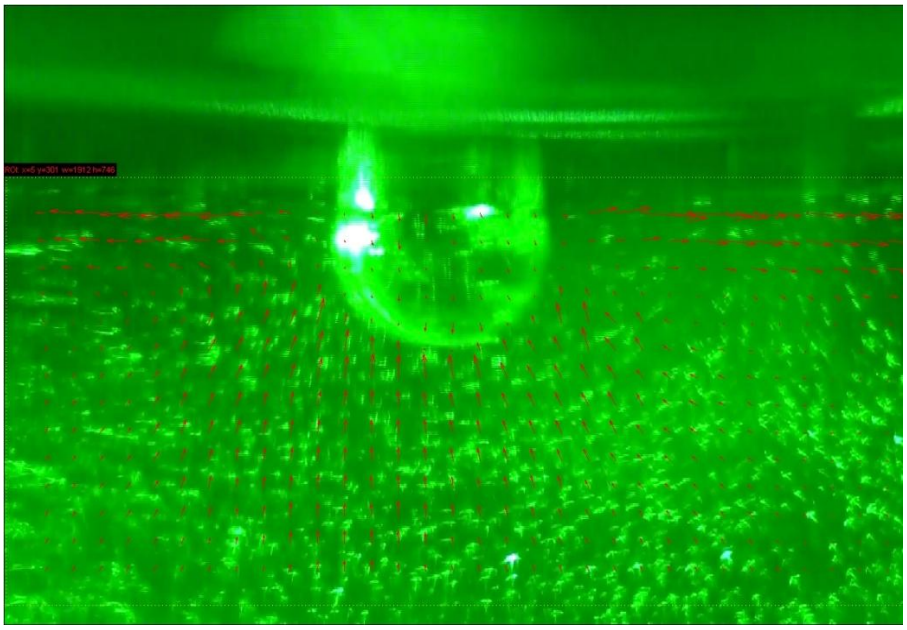

g) t = 0.55 s. The flow pattern is qualitatively similar to the previous photograph. The average velocity of the field is 0.977 mm/s.

h) t = 0.6 s. The flow pattern is qualitatively similar to the previous two photographs. The average velocity of the field is 0.99750 mm/s.

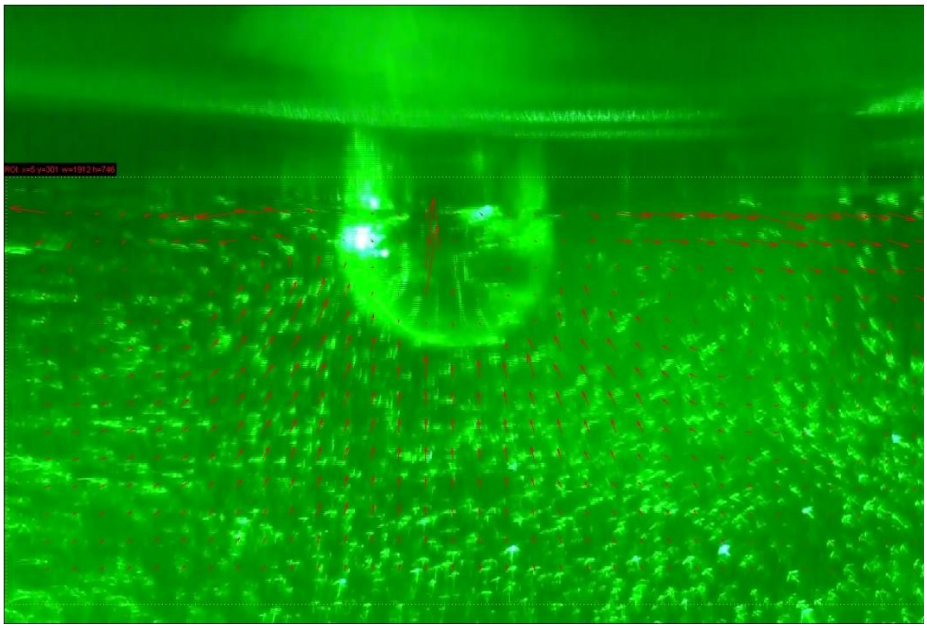

i) t = 0.65 s. The flow pattern is qualitatively similar to the photographs. The fluid velocity is decreasing with time. The average velocity of the field is 0.952 mm/s.

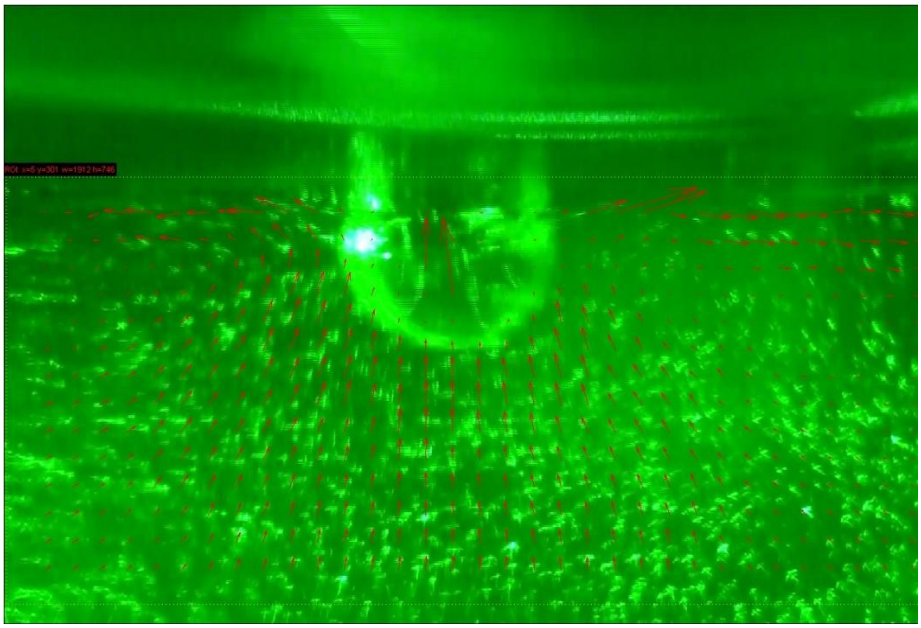

j) t = 0.70 s. The flow pattern remains qualitatively similar for the remaining photographs, but the fluid velocity is decreasing with time. The average velocity of the field is 1.07 mm/s.

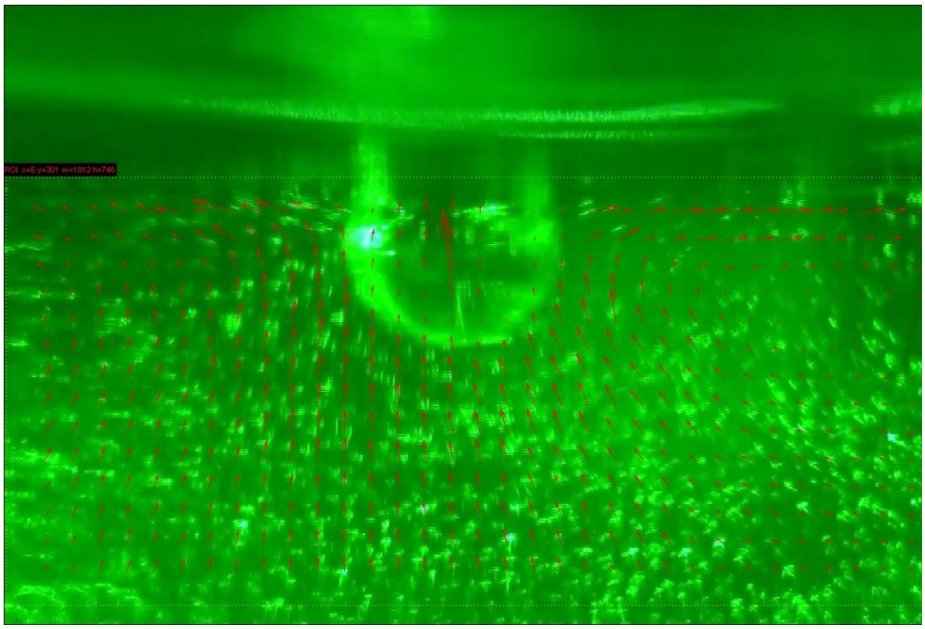

k) t = 0.78 s. The flow pattern is qualitatively similar to the photographs. The average velocity of the field is 1.38 mm/s.

6.4.3 Time Variation of Velocity Near a Test Particle

To further describe the time variation of the fluid velocity induced due to the adsorption of a particle, in Figure 6.10 the velocity at three fixed points near the particle is plotted as a function of time. The locations are shown in Figure 6.9. Datapoint A and B were close to the interface, approximately 0.2 mm from the surface of the particle. Datapoint C is below the test particle along its vertical axis 0.2 mm from the surface of the test particle. The velocities computed at those datapoints comprise of average value of 9 vectors of a frame, averaged over 7 frames.

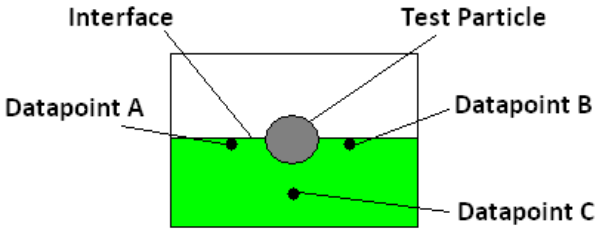

Figure 6.9 Location of Datapoints A, B and C in the laser plane. Datapoints A and B are 0.1 mm from the interface on either side of the test particle and Datapoint C is below test particle. They are at a distance of 0.2 mm from the edge of the test particle.

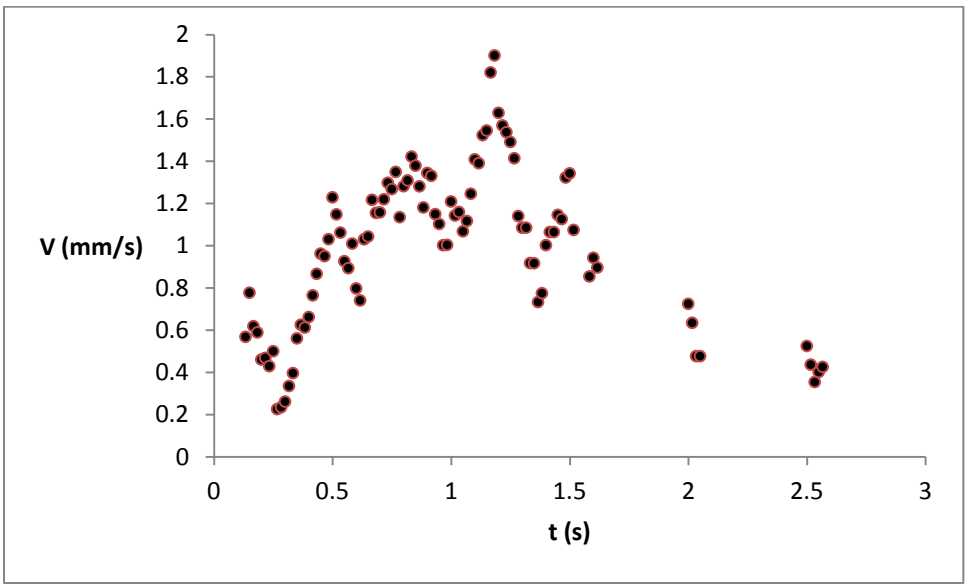

a) Datapoint A is located 0.2 mm from the interface, 0.2 mm from the surface of the particle on the left side.

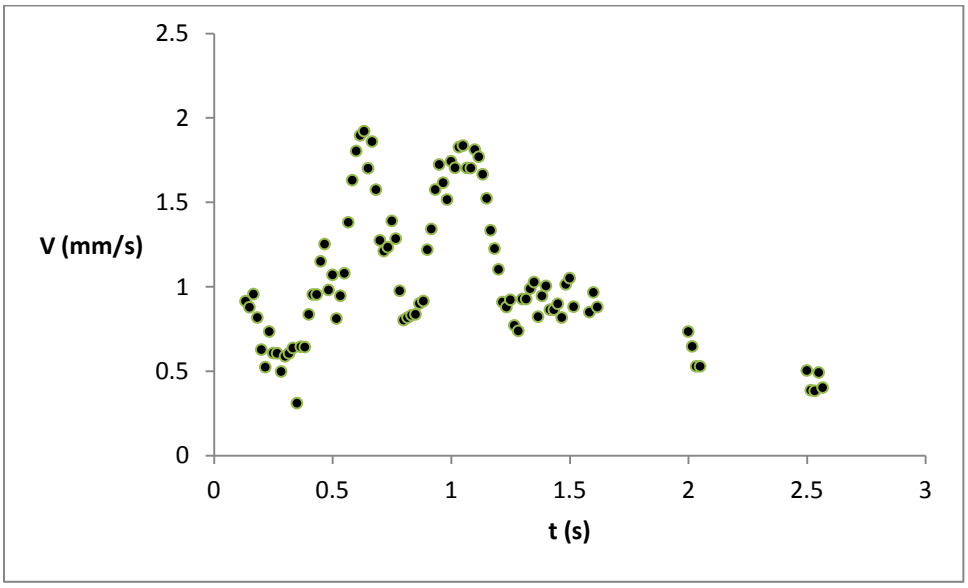

b) Datapoint B is located 0.2 mm from the interface, 0.2 mm from the surface of the particle on the right side.

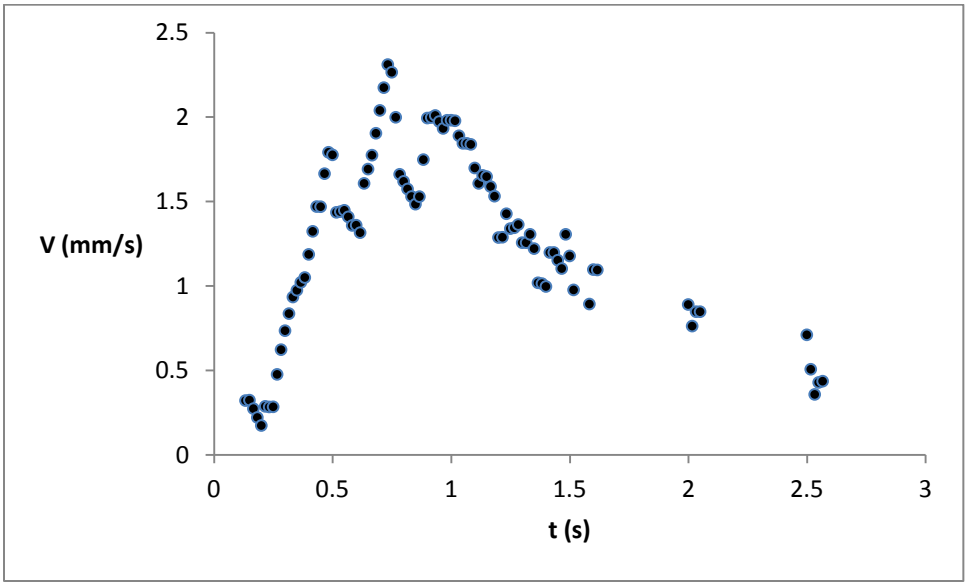

c) Datapoint C is located below the test particle, 0.2 mm from the bottom surface of the particle.

Figure 6.10 Time variation of the fluid velocity near a newly adsorbed test particle. The parameters are the same as in Figure 6.5. (a) The velocity at point A, (b) the velocity at point B and (b) the velocity at point C. The points are marked in Figure 6.9. The fluid velocity at each of the points quickly increases to a maximal value and then slowly decreases with time.

The Figure 6.10 shows that the fluid velocity increases rapidly as the test particle touches the interface. The velocity on the interface as well as below the interface is sustained for about 1 second. Then the velocity decays gradually.

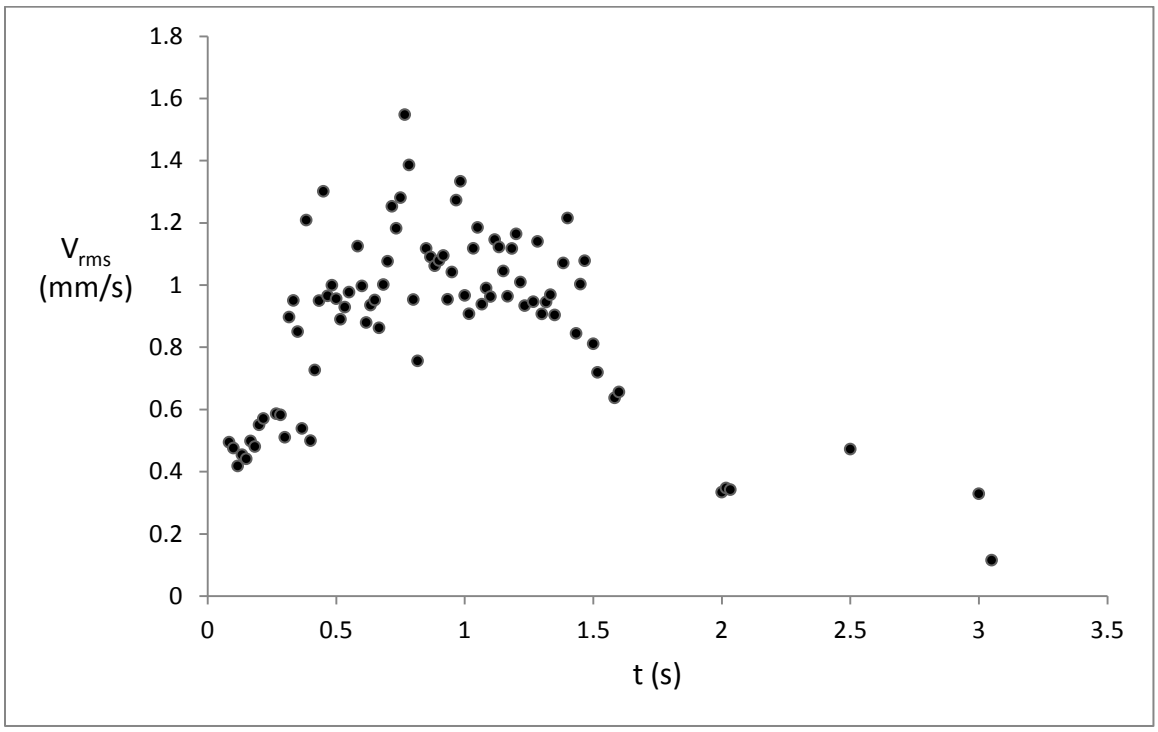

Figure 6.11 This figure represents the root mean square value of all velocity vectors in the flow field as a function of time.

The Figure 6.11 shows the rms velocity for the entire flow field as a function of time. The velocity increases to approximately 1.6 mm/s in 0.5 second. This rms value is approximately maintained for 1 second, and then the flow velocity decays with time. At about 3 s the velocity is close to 0.5 mm/s. This shows that the flow induced below the interface as a particle is adsorbed on the interface has a larger time scale compared to the flow induced on the interface. This flow below the interface starts later on and is sustained for longer period of time.

CHAPTER 7

CONCLUSIONS

The results presented in this dissertation show that the adsorption of particles onto a fluid-liquid interface can be a rather violent process. The newly-adsorbed particles not only create interfacial waves, but also cause particles already adsorbed on the interface to move away. A newly-adsorbed particle creates a circular particle-free region around itself, the radius of which can be several times larger than its own radius.

Consequently, although inertia can be usually neglected for a colloidal particle fully immersed in a fluid, this may not be case for a particle trapped at a fluid-liquid interface even when its size is as small as a few nanometers. Furthermore, for an adsorbed particle there are characteristic linear and rotational frequencies that can be excited by an external forcing. This latter behavior of particles is similar to that of an under-damped mass-spring-dashpot system.

In conclusion, it is shown that the behavior of particles adsorbed at fluid-liquid interfaces in the direction normal to the interface is different from that in the lateral direction to the interface. This is a consequence of the fact that particles are free to move laterally on the interface just like when they are fully immersed in a fluid, but in the direction normal to the interface the capillary force keeps them at their stable positions in the interface.

REFERENCES

1. Wan, J., and Wilson, J.L. (1994). Visualization of the role of the gas-water interface on the fate and transport of colloids in porous media. Water Resources Research 30(1), 11-23.

2. Diana, N., Tran, H., Whitby, C.P., and Fornasiero, D. (2010). Selective separation of very fine particles at a planar air–water interface. John Ralston International Journal of Mineral Processing 94, 35-42.

3. Abdel-Fattah, A.I., and El-Genk, M.S. (1998). On colloidal particle sorption onto a stagnant air-water interface. Advances in Colloid and Interface Science, 78, 237-266.

4. Swami, A., Kumar, A., Selvakannan, P.R., Mandal, S. and Sastry, M. (2003). Langmuir–Blodgett films of laurylamine-modified hydrophobic gold nanoparticles organized at the air–water interface. Journal of Colloid and Interface Science 260, 367-373.

5. Nudurupati, S., Janjua, M., Singh, P. and Aubry, N. (2010). Redistribution and removal of particles from drop surfaces. Soft matter 6(6), 1157-1169.

6. Aubry, N., Singh, P., Janjua, M., and Nudurupati, S. (2007). Micro- and nano-particles self-assembly for virtually defect-free, adjustable monolayers, Proceedings of the National Academy of Sciences, 106(10), 3711-3714.

7. Janjua, M., Nudurupati, S., Fischer, I., Singh, P., and Aubry, N. (2009). Electric field induced alignment and self-assembly of rods on fluid–fluid interfaces. Mechanics Research Communications 36, 55-64.

8. Singh, P., Joseph, D.D., Gurupatham, S.K., Dalal, B., and Nudurupati, S. (2009). Spontaneous dispersion of particles sprinkled onto a liquid surface. Proceedings of the National Academy of Sciences, 106, 19761-19764.

9. Gurupatham, S.K., Hossain, M., Dalal, B., Fischer, I.S., Singh, P., and Joseph, D.D. (2011). Spreading of solid powder particles over liquid surfaces. Powder Technology.

10. Balzani, V., Venturi, M., and Credi, A. (2003). Molecular devices and machines: A journey into the nanoworld. Weinheim: Wiley VCH.

11. Bowden, N. A., Terfort, A., Carbeck, J., and Whitesides, G. M. (1997). Self-assembly of mesoscale objects into ordered two-dimensional arrays. Science, 276, 233-235.

12. Grzybowski, B. A., Bowden, N., Arias, F., Yang, H., and Whitesides, G. M. (2001). Modeling of menisci and capillary forces from the millimeter to the micrometer size range. Journal of Physical Chemistry B, 105, 404-412.

13. Murray, C. B., Kagan, C. R., and Bawendi, M. G. (2000). Synthesis and characterization of monodisperse nanocrystals and close-packed nanocrystal assemblies. Annual Review of Materials Science, 30, 545-610.

14. Tang, Z., Zhang, Z., Wang, Y., Glotzer, S. C., and Kotov, N. A. (2006). Self-assembly of CdTe nanocrystals into free-floating sheets. Science, 314, 274-278.

15. Cox, P.A., and Knox, R.B. (1989). Two-dimensional pollination in hydrophilous plants: Convergent evolution in the genera Halodule (Cymodoceaceae), Halophila (Hydrocharita-ceae), Ruppia (Ruppiaceae), and Lepilaena (Zannichelliaceae). American Journal of Botany 76, 164-175.

16. Singh, P., and Joseph, D. D. (2005). Fluid dynamics of floating particles. Journal of Fluid Mechanics, 530, 31-80.

17. Singh, P., Joseph, D.D. and Aubry, N. (2010). Dispersion and Attraction of Particles Floating on fluid-Liquid Surfaces, Soft matter, 6(18), 4310-4325.

18. Gurupatham, S.K., Dalal, B., Hossain, M.S., Fischer, I.S., Singh, P., and Joseph, D.D. (2011). Particles dispersion on fluid–liquid interfaces, Particuology 9(1), 1-13.

19. Planinseka, O., Pisekb, A., and Srcicb, S. (2000). The utilization of surface free-energy parameters for the selection of a suitable binder in fluidized bed granulation. International Journal of Pharmaceutics 207 (1–2), 77-88.

20. Tuskea, Z., Regdon, G. Jr., Erosa, I., Srcicb, S., and Pintye-Hodi, K. (2005). The role of the surface free energy in the selection of a suitable excipient in the course of a wet-granulation method. Powder Technology 155(2), 139-144.

21. Buckton, Z.G. (1990). The use of surface energy values to predict optimum binder selection for granulations. International Journal of Pharmaceutics 59(2), 155-164.

22. Galet, L., Vu, T.O., Oulahna, D., and Fages, J. (2004). The wetting behaviour and dispersion rate of cocoa powder in water. Food and Bioproducts Processing 82(4), 298-303.

23. Singh, P., Joseph, D.D., Fischer, I.S., and Dalal, B. (2011). Role of particle inertia in adsorption at fluid-liquid interfaces. Physics Review Letters E, 83(4), 041606.

24. Binder, W.H. (2005). Supramolecular Assembly of Nanoparticles at Liquid–Liquid Interfaces. Angewandte Chemie International Edition 44, 5172-5175.

25. Zeng, C., Bissig, H., and Dinsmore, A.D. (2006). Particles on droplets: From fundamental physics to novel materials. Solid State Communications 139(11-12), 547-566.

26. Bresme, F., and Oettel, M. (2007). Nanoparticles at fluid interfaces. Journal of Physics: Condensed Matter 19(41), 413101.

27. Aveyard, R., Binks, B. P., and Clint, J. H. (2003). Emulsions stabilized solely by colloidal particles. Advances in Colloid and Interface Science 100, 503-546.

28. Aveyard, R., and Clint, J. H. (1996). Particle wettability and line tension. Journal of the Chemical Society: Faraday Transactions 92, 85-89.

29. Binks, B. P. (2002). Particles as surfactants—Similarities and differences. Current Opinion in Colloid and Interface Science 7, 21-41.

30. Chan, D. Y. C., Henry, J. D., and White, L. R. (1981). The interaction of colloidal particles collected at fluid interfaces. Journal of Colloid and Interface Science 79, 410-418.

31. Fortes, M. A. (1982). Attraction and repulsion of floating particles. Canadian Journal of Chemistry 60, 2889-2895.

32. Gifford,W. A., and Scriven, L. E. (1971). On the attraction of floating particles. Chemical Engineering Science 26, 287-297.

33. Katoh, K., Fujita, H., and Imazu, E. (1992). Motion of a particle floating on a liquid meniscus surface. Journal of Fluids Engineering 114, 411-417.

34. Kralchevsky, P. A., Paunov, V. N., Ivanov, I. B., and Nagayama, K. (1992). Capillary meniscus interaction between colloidal particles attached to a liquid–fluid interface. Journal of Colloid and Interface Science 151, 79-94.

35. Nicolson, M. M. (1949). The interaction between floating particles. Proceedings of the Cambridge Philosophical Society, 45, 288-295.

36. Bresme, F., and Oettel, M. (2007). Nanoparticles at fluid interfaces. Journal of Physics: Condensed Matter 19, 413101.

37. Kralchevsky, P. A., and Denkov, N. D. (2001). Capillary forces and structuring in layers of colloid particles. Current Opinion in Colloid and Interface Science 6, 383-401.

38. Lehle, H., and Oettel, M. (2007). Importance of boundary conditions for fluctuation induced forces between colloids at interfaces. Physical Review E 75, 011602.

39. Paunov, V. N., Kralchevsky, P. A., Denkov, N. D., and Nagayama, K. (1993). Lateral capillary forces between floating submillimeter particles. Journal of Colloid and Interface Science 157, 100-112.

40. Stamou, D., Duschl, C., and Johannsmann, D. (2000). Long-range attraction between colloidal spheres at the air–water interface: The consequence of an irregular meniscus. Physical Review E 62, 5263-5272.

41. De-Graaf, J., Dijkstra, M. and van Roij, R. (2009). Triangular tessellation scheme for the adsorption free energy at the liquid-liquid interface: Towards nonconvex patterned colloids. Physical Review E 80, 051405; 41.

42. Crowe, C. Multiphase Flows with Droplets and Particles. CRC, Boca Raton, FL, 1998.

43. Fan, L.S., and Zhu, C. Principles of Gas-Solid Flows. Cambridge University Press, Cambridge, UK, 1988.

44. Currie, I.G. Fundamentals Mechanics of Fluids. McGraw-Hill, New York, 1974.

45. Dhont, J.K.G. An Introduction to Dynamics of Colloids. Elsevier, Amsterdam, 1996.

46. Tsujii, K. Surface Activity: Principles, Phenomena, and Applications. Academic, New York, 1998.

47. Raffel, M., Willert, C., and Kompenhans, J., Particle Image Velocimetry: A Practical Guide Experimental Fluid Mechanics. Springer, 2002.